1   **Structure and mechanism of Zorya anti-phage defense system**

2

3   Haidai Hu[1], Thomas C.D. Hughes[2], Philipp F. Popp[3], Aritz Roa-Eguiara[1], Freddie J.O. Martin[1],
4   Nicole R. Rutbeek[1], Ivo Alexander Hendriks[4], Leighton J. Payne[2], Yumeng Yan[1], Victor Klein de
5   Sousa[1], Yong Wang[5], Michael Lund Nielsen[4], Richard M. Berry[7], Marc Erhardt[3,8], Simon A.
6   Jackson[2]*, Nicholas M.I. Taylor[1]*

7

8   [1]Structural Biology of Molecular Machines Group, Protein Structure & Function Program, Novo
9   Nordisk Foundation Center for Protein Research, Faculty of Health and Medical Sciences,
10   University of Copenhagen, Blegdamsvej 3B, 2200 Copenhagen, Denmark.

11

12   [2]Department of Microbiology and Immunology, University of Otago.

13

14   [3]Institute for Biology/Molecular Microbiology, Humboldt-Universität zu Berlin, Philippstr. 13,
15   10115 Berlin, Germany.

16

17   [4] Proteomics program, Novo Nordisk Foundation Center for Protein Research, Faculty of Health
18   and Medical Sciences, University of Copenhagen, Blegdamsvej 3B, 2200 Copenhagen, Denmark.

19

20   [5]College of Life Sciences, Zhejiang University, Hangzhou 310027, China.

21

22   [6]Department of Plant and Environmental Sciences, University of Copenhagen, Frederiksberg C,
23   Denmark.

24

25   [7]Department of Physics and Kavli Institute for Nanoscience Discovery, University of Oxford,
26   Oxford, United Kingdom.

27

28   [8]Max Planck Unit for the Science of Pathogens, Berlin, Germany.

29

30   *Correspondence: Simon Jackson, simon.jackson@otago.ac.nz
31   Nicholas Taylor, nicholas.taylor@cpr.ku.dk

32

33

34

Summary

Zorya is a recently identified and widely distributed bacterial immune system, which protects against phage invasion. It consists of a predicted membrane-embedded complex (ZorAB) and soluble components that differ among Zorya subtypes, notably ZorC and ZorD, in type I Zorya systems. Here, we reveal the molecular basis of the Zorya defense system using cryo-electron microscopy, mutagenesis, fluorescence microscopy, proteomics, and functional studies. We demonstrate that ZorAB shares the stoichiometry of other 5:2 inner membrane ion-driven rotary motors. Additionally, $ZorA_5B_2$ features a dimeric ZorB peptidoglycan binding domain and a pentameric α-helical coiled-coil tail made of ZorA that projects approximately 700 Å into the cytoplasm. We further characterize the structure and function of the soluble Zorya components, ZorC and ZorD, and find that they harbour DNA binding and nuclease activity, respectively. Comprehensive functional and mutational analyses demonstrates that all Zorya components work in concert to protect bacterial cells against invading phages. We present evidence that ZorAB operates as an ion-driven motor that becomes activated and anchors to the cell wall upon sensing of cell envelope perturbations during phage invasion. Subsequently, ZorAB transfers the phage invasion signal through the ZorA cytoplasmic tail to the soluble effectors, which function to prevent phage propagation. In summary, our study elucidates the foundational mechanisms of Zorya function and reveals a novel triggering signal for the rapid activation of an anti-phage defense system.

Introduction

Bacteria and Archaea are frequently attacked by bacteriophages (or phages). Microbes have developed an array of defense strategies to counteract these phage infections[1–3]. Such defense strategies include restriction-modification (R-M) systems that target phage genomic DNA; CRISPR-Cas systems, offering sequence-specific acquired immunity that enables cells to recognize, remember previous and combat future phage infections; abortive infection (Abi) systems that lead to metabolic arrest or cell death upon phage invasion, as well as other defense systems with mechanisms which have only recently begun to be uncovered[4,5]. Anti-phage defense systems not only play a pivotal role in regulating bacterial populations by balancing phage-host dynamics but also present great opportunities for the development of novel biotechnological tools[6]. Recently, through systematic analysis of microbial genomes, several new gene families that protect against phage infections have been identified[7–10]. Further studies have provided key insights into how these defense systems are triggered. These triggering factors commonly include phage structural components, other phage-encoded proteins, or phage nucleic acids that are recognized directly or indirectly by host defense proteins[11,12]. Considering that the initial steps of phage invasion involve interactions with the cell envelope, some defense systems may detect signals originating from the changes in the cell envelope during the early stage of infection. However, such defense mechanisms have so far remained elusive.

Among the most widespread of many recently discovered anti-phage defense systems are the Zorya systems, for which three subtypes have been identified[7,8]. Shared among all Zorya subtypes are two membrane proteins, ZorA and ZorB, which are proposed to form an oligomeric channel complex and contain domains related to the bacterial flagellar stator unit MotAB[7]. Integral to the cytoplasmic membrane, MotAB utilizes the proton-motive force across the inner membrane to drive rotation of the bacterial flagellum[13–16]. In addition to the proposed membrane complex, Zorya defense systems contain one or two cytosolic proteins with limited similarity to other proteins and hitherto unknown functions. These soluble proteins vary among different subtypes, with type I Zorya systems harboring ZorC and ZorD. Displaying limited homology with MotA and MotB, ZorA and ZorB in combination with their respective intracellular Zorya proteins, presumably have evolved and acquired adaptations to counter phage infection.

Of the few characterized bacterial immune systems that contain membrane-associated proteins, most appear to employ defense mechanisms wherein activation of membrane-anchored proteins disrupts or depolarizes the host cell membrane[5,17]. This membrane interference leads to the death or dormancy of infected cells before phages complete their replication cycle, preventing the release of viable progeny, a mechanism typically termed abortive infection[18]. An alternative to abortive infection is direct defense, in which a defense system clears an infection without causing host cell death or dormancy. It has been suggested that ZorAB may function as an ion channel that facilitates membrane depolarization during abortive infection[7]. However, it has not been ruled out that

95 ZorAB could instead act as the sensor of infection, and the molecular details and functional
96 mechanisms of Zorya systems remain to be elucidated.
97
98 In this study, we combined single-particle cryogenic electron microscopy (cryo-EM), mutagenesis,
99 functional assays, proteomics, and total internal reflection fluorescence microscopy to decipher
100 several key aspects of the Zorya defense mechanism. We discovered that ZorA and ZorB form a
101 unique 5:2 ion-driven motor complex in the inner membrane that contains a long, intracellular tail
102 structure. We provide evidence that Zorya is a direct defense system, where ZorAB is a sensor
103 responsible for detecting phage-induced perturbations of the cell envelope. During sensing of
104 phage invasion, we propose that the dimeric ZorB peptidoglycan-binding domain anchors the
105 ZorAB complex to the cell wall near the phage injection site and that the ion-driven motor rotates
106 the ZorA tail within the cytosol. The rotation would then transmit the invasion signal to the effector
107 subunits ZorC and ZorD, with ZorD being recruited to the site of activated ZorAB. ZorC and ZorD
108 display *in vitro* DNA binding and autoinhibited nuclease activity, respectively. Together, activated
109 ZorC and ZorD target and degrade the invading phage DNA within the proximity of the ZorA tail,
110 thereby preventing phage propagation. A long rotating tail-spike located close to the site of phage
111 DNA injection is strongly suggestive of a "bobbin" around which the invading DNA could be
112 wound, thereby immobilizing it for subsequent degradation.

Results

Zorya has broad activity against phage invasion through a direct immunity mechanism.

Type I and II Zorya systems are widely distributed across Gram-negative phyla, whereas type III Zorya appears to primarily occur within *Pseudomonadota* (**Fig. 1a**). Intriguingly, Zorya is rarely found in Gram-positive bacteria. To better understand the Zorya anti-phage defense mechanism, we investigated the activity of an *E. coli* type I Zorya system (*Ec*ZorI). We cloned the complete *Ec*ZorI operon from strain NCTC9026, including its native promoter, into a low copy plasmid (pACYC) and used a heterologous *E. coli* strain (MG1655 ΔRM) to examine *Ec*ZorI-mediated anti-phage defense against a panel of 70 phages[19]. The *Ec*ZorI system provided anti-phage activity against a diverse range of phages, including different families (**Fig. 1b**). Phage adsorption was not affected by *Ec*ZorI, indicating that anti-phage defense occurs at a subsequent stage of infection (**Fig. 1c**). *Ec*ZorI also prevented the phage burst of infected cells (**Fig. 1d**). We next examined whether *Ec*ZorI affected incoming DNA during bacterial conjugation or plasmid transformation but found no evidence of *Ec*ZorI defending against these mechanisms of foreign DNA uptake (**Extended Data Fig. 1a, b**). Therefore, our findings indicate that some aspect of phage infection, other than the mere introduction of foreign DNA into the cell, is required to trigger Zorya activity.

Next, we examined whether the *Ec*ZorI system provided population-level defense in liquid cultures infected at different multiplicities of infection (MOI) (**Fig. 1e** and **Extended Data Fig. 1c**). Although each phage tested affected the control populations to differing extents, population growth in the *Ec*ZorI samples was generally unaffected at low (<0.1) MOI and in some cases also high (>1) MOI. Importantly, the growth kinetics at early timepoints did not reveal any premature host population collapse or delayed growth for cells expressing *Ec*ZorI compared to the empty vector controls, as might be expected for abortive defense mechanisms. Phages were detectable at the end timepoints in most infected cultures, but at lower levels in the presence of *Ec*ZorI (**Fig. 1f and Extended Data Fig. 1d**). These findings suggest the *Ec*ZorI system does not act via an abortive infection mechanism, where induced cell dormancy or death of infected cells leads to phage extinction and population-level protection. To test this further, we measured the survival rate of cells infected with Bas24 and found that *Ec*ZorI increased cell survival, again consistent with a direct defense mechanism rather than abortive infection (**Fig. 1g**).

Figure 1. Zorya has broad activity against phages via a direct immunity mechanism.

a, Zorya phylogenetic tree. As ZorA and ZorB are present in all Zorya types, the tree was generated using concatnated ZorA+B sequences. The outer ring represents the Zorya types I, II or III, and the inner ring represents the taxonomy of bacteria. The taxonomic rank being highlighted is at the phylum level. On the right, the gene organization of the three Zorya types is shown. **b**, *Ec*ZorI defense against diverse *E. coli* phages, determined using efficiency of plaquing (EOP) assays. AAI: Average amino acid identity. **c**, Adsorption of phage Bas24 to *E. coli* cells possessing or lacking *Ec*ZorI. **d**, One-step phage growth curve for phage Bas24 infecting *E.coli*, with or without *Ec*ZorI, normalized to the plaque forming units (PFU) per mL at the initial timepoint. **e**, Infection time courses for liquid cultures of *E. coli*, with and without *Ec*ZorI, infected at different multiplicities of infection (MOI) of phage Bas24. **f**, Phage titers at the end timepoint for each sample from the infection time courses (e), measured as EOP on indicator lawns of *E. coli* either without (control) or with *Ec*ZorI. The limit of detection (LOD) is shown with dotted lines. **g**, Survival of *E. coli* cells, lacking or possessing *Ec*ZorI, infected at an MOI of 5 with Bas24. In panels **b-d**, data represent the mean of at least three replicates and error bars (**c,d**) or shaded regions (**e**) represent the standard error of the mean (SEM).

162

163   *Zorya contains a ZorA$_5$B$_2$ complex with a unique intracellular tail.*

164

165   To elucidate the molecular assembly of ZorA and ZorB, we determined the structure of the *Ec*ZorI
166   ZorA and ZorB complex (*Ec*ZorAB) using single-particle cryo-EM. We expressed then purified
167   the *Ec*ZorAB complex from cell membranes using the mild detergent lauryl maltose neopentyl
168   glycol (LMNG) (**Fig. 2a** and **Extended Data Fig. 2a**). Visualized by negative stain EM, *Ec*ZorAB
169   appeared to contain a 'head' domain attached to a long tail-like structure measuring approximately
170   700 Å (**Fig. 2b**). We then resolved the *Ec*ZorAB cryo-EM structure to an overall resolution of 2.7
171   Å (**Extended Data Fig. 2b-c** and **Extended Data Table 1**). The EM reconstruction reveals an
172   oligomeric complex consisting of five ZorA subunits and two ZorB subunits, with the same
173   stoichiometry and arrangement in the membrane as the flagellar stator unit MotA–MotB complex
174   (MotA$_5$B$_2$)[15] (**Fig. 2c-e, h**). Quantitative mass spectrometry analyses of *Ec*ZorI-expressing *E. coli*
175   cells support the 5:2 ZorA:ZorB ratio (**Extended Data Fig. 2k, l** and **Extended Data Table 2**).
176   Overall, *Ec*ZorAB comprises four distinct structural layers: a peptidoglycan binding domain
177   (PGBD, ZorB residues T47-L246), transmembrane domain (TMD), membrane-proximal
178   cytoplasmic domain (MPCD), a region spanning ZorA residues G48-L127, K207-S222), and a
179   tail-like structure formed by the ZorA C-terminal region (ZorA residues G223-T729) (**Fig. 2a**, **2d**).
180

181   The periplasmic region of the complex exhibits flexibility relative to the TMD. Nevertheless, local
182   refinement improved the resolution to 3.5 Å, clearly resolving a dimerized ZorB PGBD (**Extended**
183   **Data Fig. 2h-j**). The resolution corresponding to the TMD and MPCD reached 2.2 Å, allowing us
184   to model sidechain rotamers and non-protein molecules such as water, ions and lipids. For the
185   ZorA tail, our cryo-EM map provides density information for the first 56 residues. Mass
186   spectrometry analyses on the purified *Ec*ZorAB complex confirmed the presence of the intact
187   ZorA C-terminal region, consistent with the negative stain images, but conformational
188   heterogeneity prevented 3D reconstruction of the entire ZorA tail (**Fig. 2b-d** and **Extended Data**
189   **Fig. 3a**). Secondary structure prediction revealed a preference for the tail to adopt α-helical
190   structures, suggesting that the rest of the ZorA tail is likely to be a continuation of the
191   experimentally determined structure, which folds into a coiled coil with a right-handed super-
192   helical twist towards cytoplasm (**Extended Data Fig. 3a**). Additionally, we observed a consistent
193   hydrophobic pattern in the tail sequence (**Extended Data Fig. 3c, d**). Based on these observations,
194   we constructed an idealized full-length ZorA model where the ZorA tail forms a helical bundle
195   projecting into the cytoplasm, having a helical pitch of 328 Å and a radius of 9.0 Å (**Fig. 2l** and
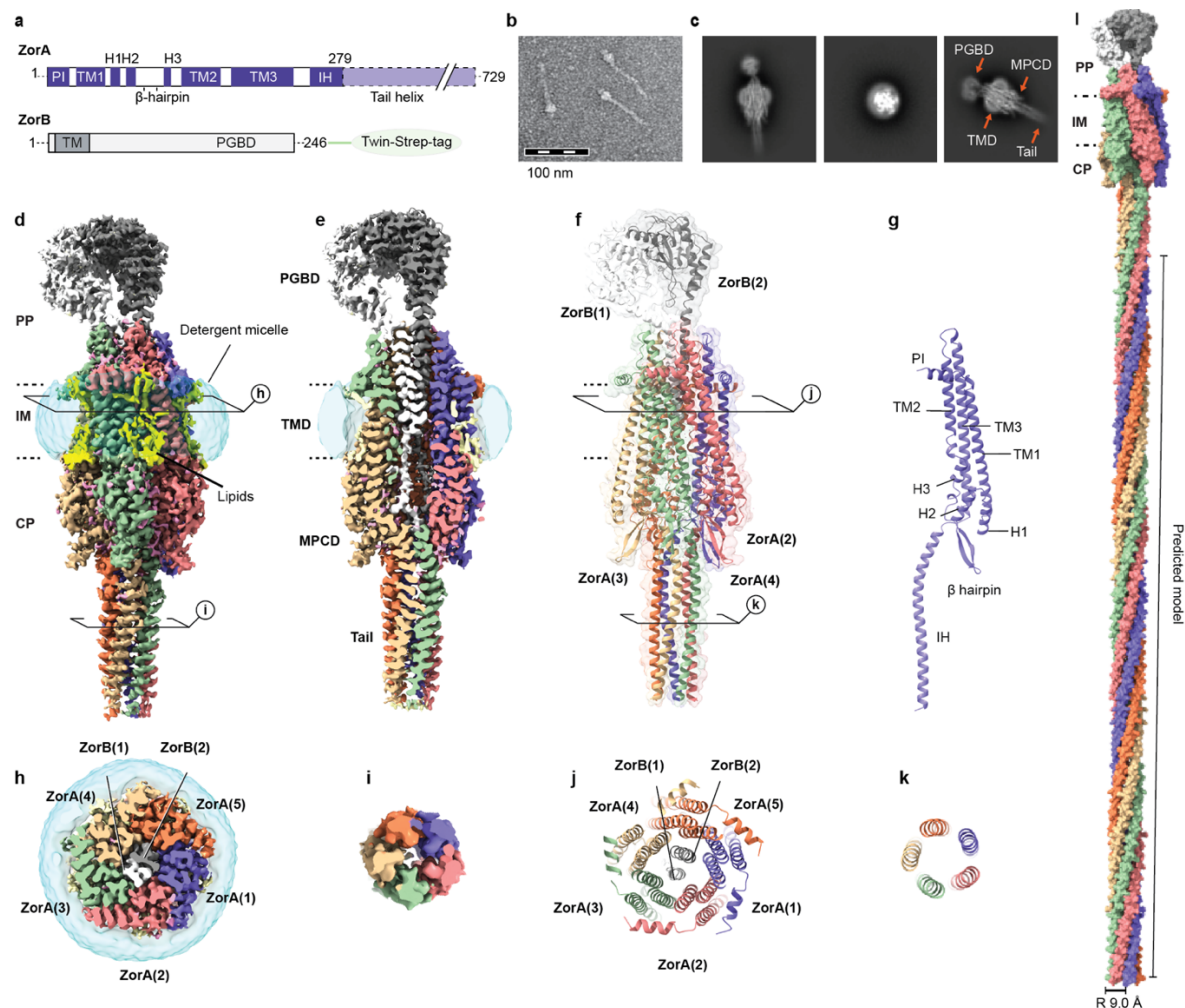196   **Extended Data Fig. 3c**).

Figure 2. Cryo-EM of *Ec*ZorAB and its architecture.

a, Schematic representation of *Ec*ZorA and *Ec*ZorB. **b,** Negative staining image of purified *Ec*ZorAB particles. **c**, Representatives of high-resolution 2-dimensional classes of *Ec*ZorAB particles from cryo-EM. Domain architectures of the E*c*ZorAB complex are depicted. **d**, Cryo-EM map of *Ec*ZorAB. Five ZorA subunits (purple, salmon, light green, tan, and coral) surround two ZorB subunits (white and dark gray) viewed from the plane of the membrane. Membrane-bound lipids are shown in yellow. The detergent micelle is shown as a translucent surface representation in cyan. Dashed lines depict inner membrane boundaries. **e**, Cross-section view of the EM density map. **f**, Ribbon model representation of *Ec*ZorAB. **g**, Structure of a single ZorA subunit. **h-i**, Cross-section view of the Cryo-EM map of *Ec*ZorAB TMD (**h**) and tail (**i**) from the periplasmic side. **j-k**, Cross-section view of the model of *Ec*ZorAB TMD (**j**) and tail (**k**) from the periplasmic side. **l**, Composite model of *Ec*ZorAB whole complex. the predicted portion of the ZorA tail is represented as surface. The radius of the ZorA tail is shown in **l**. PP, periplasm; IM, inner membrane; CP, cytoplasm; PGBD, peptidoglycan binding domain; TMD, transmembrane domain; MPCD, membrane-proximal cytoplasmic domain; TM, transmembrane; H, helix.

213

214   *ZorAB is a peptidoglycan-binding rotary motor*

215

216   On the periplasmic side, the C-terminal PGBDs of the two ZorB subunits form a homodimer, with
217   each monomer consisting of four helices (α1-α4) and an antiparallel β-sheet (β1-β5) (**Fig. 3a** and
218   **Extended Data Fig. 4a, b**). The dimerization interface is composed of α3 and β5 from each
219   monomer, driven mainly by van der Waals forces and electrostatic interactions. Additionally, a C-
220   terminal loop from ZorB caps the side of the dimerization interface (**Fig. 3b**). Each monomer
221   contains two disulfide bridges resolved in the cryo-EM density: one connects the α1 and β1-β2
222   loops, and the other connects α3 and the ZorB C-terminal end, potentially contributing to the
223   folding, stability and rigidity of the ZorB PGBDs (**Fig. 3b** and **Extended Data Fig. 4c, d**). The
224   overall ZorB dimer structure resembles that of the periplasmic domain of the flagellar stator units
225   MotB, and other peptidoglycan (PG) binding proteins[20,21] (**Extended Data Fig. 4b**). MotAB is
226   kept in an inactive state by the MotB 'plug' regions (following the TMD and preceding the PGBD)
227   that inhibit ion flux and rotation of MotA around MotB (**Extended Data Fig. 4f, g**). Only upon
228   incorporation of MotAB into the flagellar motor is the MotB plug released and the PGBDs
229   dimerize to enable PG binding[15]. Intriguingly, in our structure the ZorB PGBD is already
230   dimerized and purified ZorAB can bind PG (**Extended Data Fig. 4e**).

231

232   In the ZorAB TMD, two ZorB transmembrane helices (TM) are asymmetrically surrounded by
233   five ZorA subunits. Each ZorA subunit consists of three transmembrane helices (TM1-TM3).
234   ZorA TM2 and TM3 are lined directly against ZorB TM, while TM1 is peripheral and faces the
235   lipid bilayer (**Fig. 2g**). Lipid densities are observed in the EM reconstruction on both leaflets of
236   the membrane (**Extended Data Fig. 2f, g**). These protein-bound lipids likely stabilize the TMD
237   and enhance the oligomeric assembly. The TMD of ZorAB is structurally related to that of 5:2 ion-
238   driven prokaryotic rotary motors, including possessing the universally conserved and
239   mechanistically important aspartate residue, D26 in ZorB. One ZorB D26 is engaged with ZorA
240   chain C TM2 T147 and TM3 S184 and the other D26 is unengaged and points toward a lumen
241   enclosed by the ZorA MPCD (**Fig. 3a, d**). The interaction modes of these two D26 are the same
242   as those in the inactive state of MotAB, suggesting similar working mechanisms (**Extended Data
243   Fig. 4h-j**). Additionally, we do not find any region corresponding to a 'plug' in ZorB. However,
244   we do observe that P163 from ZorA(2) (ZorA chain 2) induces a kink in ZorB(1) α1 near residue
245   46, and two pairs of salt bridges (ZorA(2) E164-ZorB(1) R49; ZorA(5) E164-ZorB(2) R52) and
246   several polar interactions are located at the ZorAB periplasmic assembly interface that might block
247   the rotation of ZorA around ZorB in this conformational state (**Fig. 3a, c**). In support of a rotation-
248   suppressing role, when we replaced ZorB residues 46-52 with a GGGSGGS linker we were able
249   to generate a nearly identical Cryo-EM reconstruction to the WT complex, apart from the
250   unresolved density of ZorB TMDs and the flexible ZorB PGBDs (**Extended Data Fig. 4m-q**),
251   which is consistent with freedom of ZorA to rotate around ZorB (through Brownian motion) in the
252   mutant.

253

254   On the cytoplasmic side, the ZorA TMD and MPCD are directly connected by TM1 and TM3, the
255   intracellular segments of which are joined by three vertical helices (H1-H3) and a β-hairpin motif
256   (**Fig. 2g**). H3 is less ordered due to the presence of two proline residues, P126 and P136. We found
257   five strong, spherical densities in the ZorA MPCD, each coordinated by the mainchain carboxylate
258   groups of S218 and Y220 at the end of TM3, and the side chains of E86 and E87 from the adjacent
259   subunit, as well as two well-resolved water molecules (**Fig. 3a, e**). Based on the strongly negative
260   electrostatic environment and the surrounding coordinating residues, we assigned this density to a
261   Ca^{2+}, which bridges the MPCD of two adjacent ZorA subunits and links ZorA TM3 to its
262   intracellular helix (**Fig. 3e** and **Extended Data Fig. 5b**).

263

264   Consistent with a function for ZorAB as an ion-driven rotary motor, we observed a water-filled
265   ion permeation pathway connecting the periplasmic space, via the unengaged ZorB D26, to the
266   cell cytosol (**Fig. 3g**). On the periplasmic side, a cavity is lined by the end of TM2, the beginning
267   of TM3, and the turn between the ZorA periplasmic interface (PI) helix and TM1. Several
268   negatively charged residues are found in this region, which join to create a negatively charged
269   environment that would attract incoming ions (**Fig. 3g**). Moving towards the cytoplasmic side,
270   ZorA residues T147 and S184 resemble an ion selectivity filter[16] that controls ion access from the
271   periplasm to ZorB D26 (**Fig. 3d, g**). The absence of the additional polar residues in the ion
272   selectivity filter strictly required for sodium coordination indicates that ZorAB is likely a proton-
273   driven motor[16] (**Extended Data Fig. 4h-j**). The pathway extends from ZorB D26 in the direction
274   of the cytoplasm to the inner lumen encircled by the ZorA MPCD. We found lateral portals in the
275   ZorA MPCD, framed on one side by H2 and the broken H3, and on the other side, by the
276   intracellular part of TM3 from the neighboring subunit. The portal is beneath the head of the
277   membrane-bound lipids and above the Ca^{2+}-binding site, and it is highly hydrated, which could
278   facilitate ion exit (**Fig. 3g**). Taken together, our structural analyses and comparisons imply that
279   upon activation, the ZorAB TMD utilizes the across membrane proton gradient to drive the rotation
280   of ZorA around ZorB.

281

282   Next, we mutated residues along the ion-permeation pathway to assess the role of the ZorAB TMD
283   in Zorya anti-phage defense activity. ZorB D26 is universally conserved and essential for all
284   models of ion translocation and motor rotation. Replacement with asparagine abolishes defense
285   against phage infection (**Fig. 3d, h** and **Extended Data Fig. 6a**). In the ion-selectivity filter,
286   mutation of ZorA T147 to alanine significantly decreases defense ability. Furthermore, mutation
287   of ZorA P136, which creates a kink in the ZorA MPCD H3 helix and in turn leads to the formation
288   of an electrostatic contact between the backbone carbonyl oxygen of ZorA(4) K133 and the side
289   chain of ZorB(1) K18, to alanine results in increased defense activity (**Fig. 3g, h** and **Extended
290   Data Fig. 6a**). These observations are consistent with rotation of ZorAB, driven by ion flux
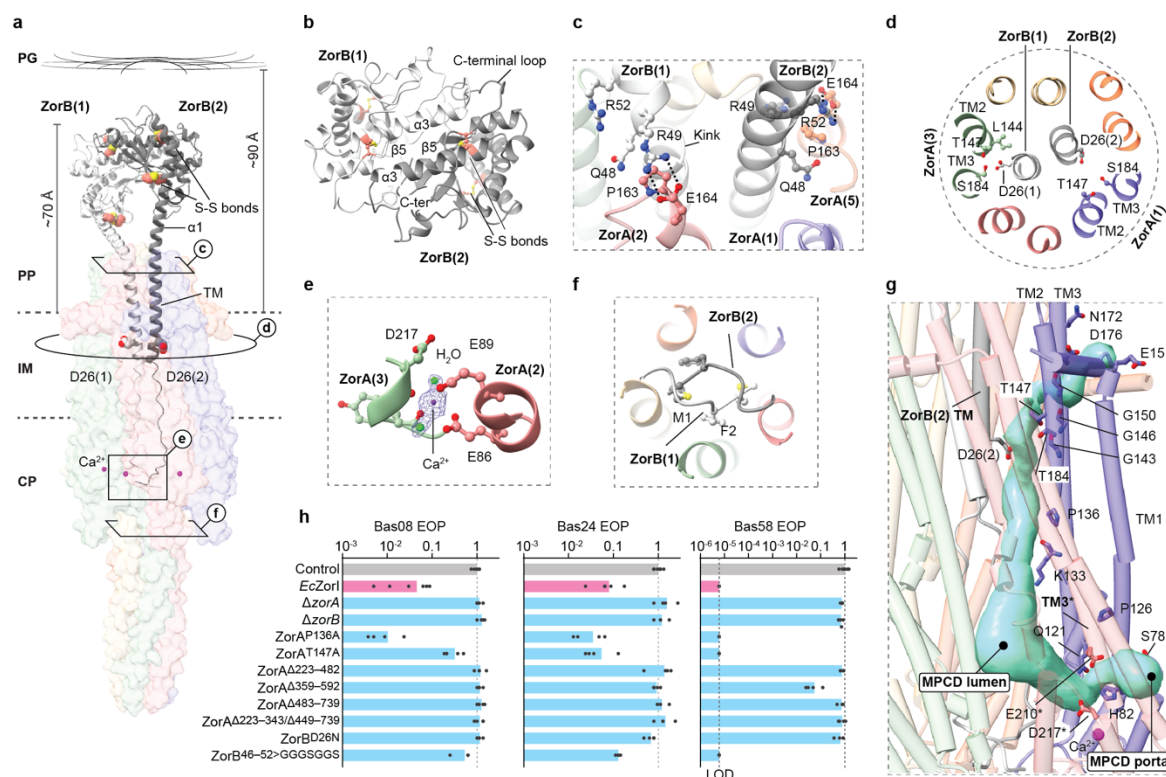291   through the above pathway, being essential for Zorya anti-phage defense.

292

Figure 3. ZorAB is a PG-binding rotary motor.

a, *Ec*ZorAB viewed from the plane of the membrane, with ZorB shown as ribbons (black and white) and ZorA shown as a translucent surface representation. The distance between the inner membrane and PG layer in *E.coli* is approximately 90 Å[68]. The cysteines from the two disulfide bridges in the ZorB PGBD are indicated and shown as spheres. The aspartate residues D26 from both ZorB TM are indicated and shown. **b**, Top view of the ZorB PGBD. **c,** Close-up view of the interactions of ZorB with ZorA at the domain assembly interface in the periplasmic space. **d,** Cross section view of ZorAB TMD, showing the ZorB D26 and surrounding residues. **e**, Ca^{2+} binding site. EM densities are only overlapped on Ca^{2+} ion, and the two water molecules. **f**, Close-up view of the interactions of the ZorB N-terminus with ZorA tail **g**, Ion translocation pathway (semitransparent surface representation in light blue) in ZorAB. Residues along the ion permeation pathway and from the ion selectivity filter are shown. Each asterisk indicates residues or structural elements from neighboring ZorA subunit. **h**, The effects of ZorA and ZorB mutations on *Ec*ZorI-mediated anti-phage defense, as measured using EOP assays. Data represent the mean of at least 3 replicates and are normalized to the control samples lacking *Ec*ZorI. For phage Bas58, the limit of detection (LOD; one plaque observed in the assay) is marked with a bashed line. In the absence of any observed plaques, the result was recorded as the LOD. ZorB$^{46\text{-}52\text{>}GGGSGGS}$ corresponds to the replacement of ZorB residues 46-52 with a GGGSGGS linker. Data for additional phages are provided in **Extended Data Fig. 6a**.

314   *ZorAB intracellular tail controls the Zorya anti-phage defense activity*

315

316   One of the most salient features of the ZorAB complex is its long tail-like structure, of which we
317   could confidently model the initial 56 residues (residues G223-T279) (**Fig. 2a, d**). Within the ZorA
318   MPCD, ZorB N-terminal residues M1 and F2 intertwine and hydrophobically block the entrance
319   of the tail (**Fig. 3f**). On the outside of the tail, residue R108 from the β-hairpin motif forms a salt
320   bridge with D22, and H92 makes electrostatic contact with the hydroxyl group of F228 (**Extended
321   Data Fig. 5a, b**). These interactions appear to be critical for the assembly of the ZorAB complex,
322   since disrupting these interactions by deleting the entire tail (residues G223-T729) abolish ZorAB
323   complex formation, and we could only purify the dimerized ZorB (**Extended Data Fig. 5e**). Inside
324   the tail there are many hydrophobic residues present. L250, L254, L258 and L261 from each ZorA
325   subunit comprise continuous hydrophobic pentameric rings. Additionally, we observe an extra
326   density along the tail central axis in this region, which is best modeled as a fatty acid, consistent
327   with a predicted lipid binding site by deep learning methods[22] (**Extended Data Fig. 5c**). Given
328   that the tail structure protrudes into the cytoplasm and is surrounded by aqueous solution,
329   hydrophobic interactions inside the tail seem to be the primary driving force for tail assembly, and
330   it is unlikely that the tail conducts ions or other small soluble molecules. Intriguingly, part of the
331   ZorA tail (residues 540-729) shows homology with the core signaling unit of the bacterial
332   chemosensory array (**Extended Data Fig. 3b**), which contains a long intracellular helical bundle
333   responsible for transferring signal from the extracellular environment into the cell and regulates
334   the activities of the subsequent effectors[23]. Sequence analyses further reveal that the length of the
335   tail appears consistent across Zorya subtypes, suggesting that a uniform tail length is functionally
336   essential (**Extended Data Fig. 6b**).

337

338   Deletion of any of the Zorya proteins results in loss of anti-phage protection, emphasizing that the
339   complete function of the Zorya system requires the presence of all its components and relies on
340   the communication between the membrane anchored ZorAB complex and cytosolic soluble
341   proteins (**Fig. 3h** and **Fig. 4c, h**). Considering the motor-like structural features of ZorAB TMD
342   and its intracellular long tail, we speculated that the ZorA tail is responsible for transmitting a
343   signal derived from the motor activity to the cytosolic proteins ZorC and ZorD. We assessed
344   whether the integrity of the ZorA tail is required for the system's function. We made four ZorA
345   tail truncations: deleting the beginning (ZorA$^{\Delta223-482}$), middle (ZorA$^{\Delta359-592}$) and tip (ZorA$^{\Delta483-729}$)
346   of the tail as well as a combination of deleting the beginning and middle (ZorA$^{\Delta223-343/\Delta449-729}$). All
347   these mutations abolish *Ec*ZorI anti-phage defense ability (**Fig 3h**, **Extended Data Fig. 5a** and
348   **Extended Data Fig. 6a**). To discern whether deletion of the middle or tip of the tail affect ZorAB
349   assembly, we further expressed and determined the structures of two ZorAB mutants (ZorA$^{\Delta359-592}$
350   and ZorA$^{\Delta435-729}$). Examination of the purified mutant samples under negative stain EM show the
351   shortened tail length (**Extended Data Fig. 5f, g**). Cryo-EM structures reveal that the two mutants
352   have similar assemblies to ZorAB WT, unlike the complete tail deletion. (**Extended Data Fig. 5h,
353   i** and **Extended Data Table 1**). Hence, truncation of the middle or the tip of the tail does not affect

354   the ZorAB TMD motor assembly or formation of the remainder of the tail bundle but does impede

355   Zorya function. Subsequently, the Ca^{2+} binding site was also investigated. Indeed, double mutation

356   of E86 and E89 to alanine results in loss of Zorya function (**Fig. 3h, Extended Data Fig. 5j** and

357   **Extended Data Fig. 6a**). Structural comparisons between the Ca^{2+} mutant and ZorAB WT reveal

358   conformational changes in the ZorA MPCD, including the linker between TM3 and ZorA tail helix

359   (**Extended Data Fig. 5d, j**). Inactive Ca^{2+} binding sites therefore likely break the connection

360   between the ZorAB TMD motor and the tail. Collectively, these results demonstrate that ZorAB

361   tail length and integrity are essential for Zorya protection from phage infection.

362

363   *ZorC and ZorD interact with DNA*

364

365   To better understand the roles of ZorC and ZorD in anti-phage defense, we next set out to obtain

366   structural models and investigate their biological roles. ZorC is a soluble protein with no predicted

367   function but possesses an EH signature motif (E400, H443). We determined the cryo-EM structure

368   of *Ec*ZorC to an anisotropic resolution of 3.7 Å (**Fig. 4a, Extended Data Fig. 7a-f** and **Extended**

369   **Data Table 1**). *Ec*ZorC consists of a 'core' domain that connects through a long linker to a C-

370   terminal globular domain. In the core domain, we mapped the EH signature motif: E400 and H443,

371   together with D332, R335, W339, and W458, form an electrostatic network that is buried in a

372   pocket at the C-terminal end of the core domain (**Fig. 4b**). This network appears to be critical for

373   Zorya function, as the individual substitution of E400 or H443 with alanine abolish Zorya defense

374   (**Fig. 4c**). Additionally, in the AlphaFold2-predicted model, the N-terminal part of *Ec*ZorC

375   (residues M1-E48) contains two helices, which are hydrophilic and diverge from the core domain;

376   however, no density is observed for this region in the resolved cryo-EM map (**Extended Data Fig.**

377   **7e, g**). For the C-terminal globular domain of *Ec*ZorC, it was not possible to build an atomic model

378   *de novo* due to its conformational flexibility. Deletion of the ZorC N-terminal two helices or of

379   the ZorC C-terminal globular domain result in loss of Zorya function (**Fig. 4c**). Analyzing the

380   electrostatic distribution of the hydrophilic surface of ZorC reveals several patches of positively

381   charged regions, including the regions adjacent to the two helices and EH signature motif

382   (**Extended Data Fig. 7h**), indicating that ZorC could interact with nucleic acids. To test this, we

383   incubated ZorC with non-specific dsDNA oligonucleotide. We observed that ZorC migrates

384   together with DNA, and at higher ratios of protein-DNA complex aggregation was observed,

385   indicating that ZorC is a DNA binding protein. Deletion of the 'cap' domain or mutations in EH

386   signature motif significantly alter the DNA binding activity of ZorC (**Fig. 4d, e**).

387   *Ec*ZorD contains 1,080 residues and has a predicted Snf2-related domain at its C-terminus[7]. This

388   domain is known for utilizing energy derived from ATP hydrolysis to bind or remodel DNA[24].

389   Therefore, we determined the structure of *Ec*ZorD, in the absence and presence of ATP-γ-S (a

390   slowly hydrolysable ATP analog), to resolutions of 2.7 Å and 2.8 Å, respectively (**Fig. 4f**,

391   **Extended Data Fig. 8b, d** and **Extended Data Table 1**). The *Ec*ZorD N-terminal domain

392   (residues M1-N502) interacts directly with its C-terminal domain (residues D503-A1080), forming

393 a toroid-shaped molecule. ATP-γ-S is bound within a cleft where the hallmark DEAQ box motif
394 (ZorD residues D730-Q733) is situated, surrounded by many conserved negatively charged
395 residues (**Fig. 4g** and **Extended Data Fig. 8f, g**). We generated Zorya mutants that encode alanine
396 substitutions in both the ZorD ATP binding site and those conserved negatively charged residues
397 to assess their role in Zorya defense (**Fig. 4g**). In agreement with structural analysis, suppressing
398 the charge of these residues resulted in loss of function of the Zorya system (**Fig. 4h**). Next,
399 purified ZorD was incubated with plasmids to assess its DNA targeting activity. We observed that
400 full-length ZorD is unable to degrade DNA. However, when we purified the ZorD N-terminal
401 domain and C-terminal domain separately, we found that ZorD C-terminal domain exhibits
402 nuclease activity that can rapidly degrade both plasmid DNA and phage genomic DNA (**Fig. 4i-4l**
403 and **Extended Data Fig. 8a**). Mutation of the residues from the DEAQ box motif (D730A, E731A)
404 or a glutamate (E651) recognizing the ribose sugar group of the ATP completely abolishes the
405 nuclease activity of the ZorD C-terminal domain (**Fig.4i-4l**). These results suggest that ZorD
406 harbors a nuclease activity, and full-length ZorD is in an autoinhibited state, which is likely
407 activated once the defense is triggered, presumably through a conformational change.
408

411 **Figure 4. Structural and functional characterization of ZorC and ZorD.**
412 **a**, Ribbon model representation of ZorC. **b**, Details of the ZorC EH signature motif. **c**, The effects
413 of ZorC mutations on *Ec*ZorI-mediated anti-phage defense, as measured using EOP assays. **d**, *In*
414 *vitro* interaction of *Ec*ZorC with 200 nM dsDNA (52bp, 5' FAM-labeled scrambled DNA

415 sequence), ZorC concentrations were from lane 2 to lane 8: 1600, 100, 200, 300, 500, 1000, and
416 1600 nM, respectively. **e**, The effects of ZorC mutations on dsDNA binding activity, all reactions
417 were made to a final concentration of 200 nM of dsDNA and 1000 nM of protein. Gels in **d** and **e**
418 are representative of three independent assays. **f**, Ribbon model representation of *Ec*ZorD in
419 complex with ATP-γ-S. *Ec*ZorD structure is shown in light purple with the bound ATP-γ-S shown
420 in spheres. **g**, The ZorD ATP-γ-S binding site. The backbone of the DEAQ box motif (ZorD
421 residues 730-733) is colored in magenta. Conserved negatively charged residues surrounding ZorD
422 DEAQ box motif is shown. **h**, The effects of ZorD mutations on *Ec*ZorI-mediated anti-phage
423 defense, as measured using EOP assays. ΔNTD represents ZorD$^{Δ1-502}$ and ΔCTD represents
424 ZorD$^{Δ503-1080}$. **i**, ZorD$_{CTD}$ degrades linear plasmid DNA. **j-l**, ZorD$_{CTD}$ degrades phage genomic
425 DNA (gDNA). For c and h, data represent the mean of at least 3 replicates and are normalized to
426 the control samples lacking *Ec*ZorI. For phage Bas58, the limit of detection (LOD; one plaque
427 observed in the assay) is marked with a bashed line. Data for additional phages are provided in
428 **Extended Data Fig. 6a**. **6d**, **6e** and **i-l** are representative of at least 3 replicates.

ZorAB recruits ZorC and ZorD during phage invasion

432 To examine how the ZorAB, ZorC, and ZorD activities are coordinated in response to phage
433 infection, we explored whether it was possible to complement deletions of the *Ec*ZorI soluble
434 components with the corresponding components of Zorya from another species. Testing a
435 *Pseudomonas aeruginosa* type I Zorya (*Pa*ZorI) cloned under the native *Ec*ZorI promoter revealed
436 defense activity against several of the same phages protected against by *Ec*ZorI (**Extended Data
437 Fig. 9**). However, neither *Pa*ZorD nor *Pa*ZorCD genes could complement deletions of the
438 corresponding *Ec*ZorI genes, hinting that direct interactions occur between at least one of ZorAB–
439 ZorC, ZorAB–ZorD, or ZorC–ZorD (**Extended Data Fig. 9**). Our quantitative mass spectrometry
440 data indicate there are ~200 *Ec*ZorAB complexes (assuming most ZorA and ZorB are assembled
441 in ZorA$_5$B$_2$ complexes), 155 *Ec*ZorC, and 165 *Ec*ZorD per cell possessing pZorI, implying an
442 approximately 1:1:1 ZorA$_5$B$_2$:ZorC:ZorD stoichiometry (**Extended Data Fig. 2j, k** and **Extended
443 Data Table 2**). We next used total-internal reflection fluorescence (TIRF) microscopy to examine
444 the sub-cellular distributions of fully functional mNeonGreen (mNG) fusions to *Ec*ZorB (ZorB-
445 mNG), *Ec*ZorC (mNG-ZorC) and *Ec*ZorD (ZorD-mNG) (**Extended Data Fig. 10a**). Expression
446 of mNG from the *Ec*ZorI promoter resulted in uniform, cytoplasmic fluorescence independent of
447 the presence of phage (**Extended Data Fig. 10b**). For ZorB, we observed a significant increase in
448 the quantity of foci, that likely comprise multiple ZorAB complexes, when the bacteria were
449 infected with Bas24 (**Fig. 5a, b**). Consistent with the anticipated integral-membrane localization,
450 the ZorAB complexes were predominately membrane-localized and exhibited low diffusibility,
451 irrespective of the presence of phage (**Extended Data Video 1** and **Extended Data Video 2**). In
452 contrast, the fluorescent foci formed by the cytosolic Zorya components ZorC and ZorD freely
453 diffused in the cytoplasm in the absence of phage (**Fig. 5c, e** and **Extended Data Video 3**).
454 However, upon phage infection, we observed a significant increase in the number of ZorC/ZorD

foci, which further appeared to become static (**Fig. 5d, f** and **Extended Data Video 4**). We presume that phage inflict damage on the cell envelope at multiple sites, which in turn activates the Zorya system to the maximum extent. The hypothesis that ZorC/D is recruited to ZorAB complexes during phage infection is reinforced by a positive correlation between the number of ZorD foci and the multiplicity of Bas24 infection (**Extended Data Fig. 10c, d**). Collectively, these results suggest that multiple ZorAB complexes detect phage infection. Subsequently, the cytosolic Zorya effectors ZorC and ZorD are recruited by ZorAB complexes to prevent phage propagation.
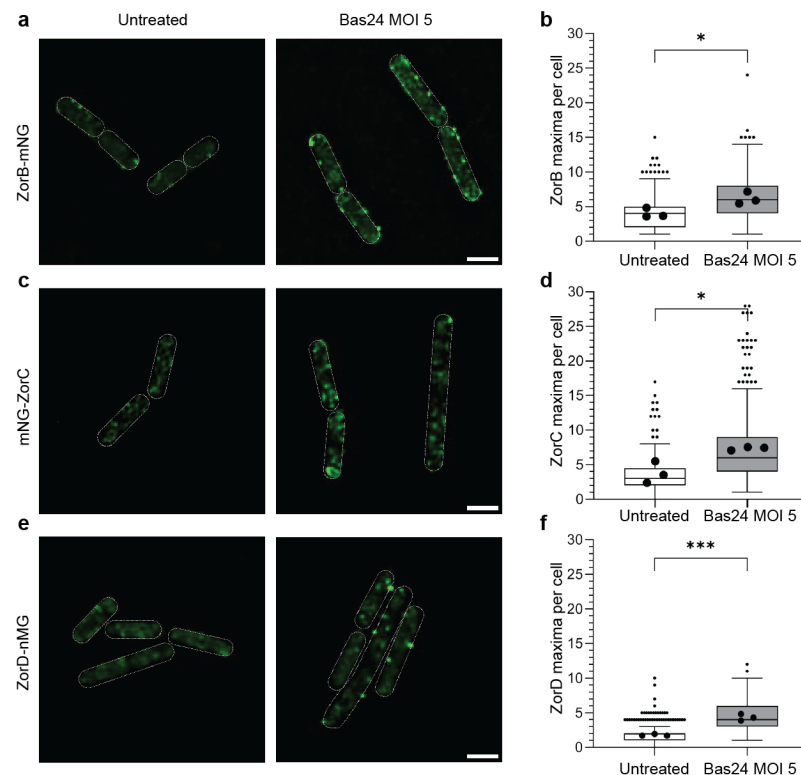
Figure 5. a, **c**, **e,** Exemplary deconvolved TIRF microscopy pictures of ZorB C-terminal, ZorC N-terminal, and ZorD C-terminal fusions with mNeongreen either untreated or exposed to Bas24 at an MOI of 5 for 30 min. **b, d, f,** Comparison of detected maxima of the ZorI proteins between untreated or exposed to Bas24 at an MOI of 5 for 30 min (n cells > 250). Means are derived from three independent biological replicates. Scale bar 2 μm. Statistics were calculated in Prism GraphPad 9 by applying the in-built analyses of unpaired t-tests or one-way ANOVA[59]. P-value: NEJM (New England Journal of Medicine) style, 0.12 ns, 0.033(*), 0.002(**), <0.001(***).

474 **Discussion**

475

476 Here, we show that an *E. coli* type I Zorya system exhibits broad defense activity against
477 phylogenetically diverse phages but not against bacterial conjugation or plasmid transformation.
478 ZorA and ZorB form an inner membrane-integrated ZorA$_5$B$_2$ proton-driven motor complex with
479 a long, intracellular tail structure. We propose that the ZorAB complex acts as a sensor to detect
480 phage-induced perturbation of the cell envelope and then transmits an invasion signal, via rotation
481 of the ZorA tail, to recruit and activate the effectors ZorC and ZorD. Activated ZorC and ZorD
482 then bind and degrade invading phage DNA within the proximity of the infection site (**Fig. 6**).

483

484 Our overall model for the Zorya anti-phage defense mechanism is more likely than alternate
485 models in which ZorC and/or ZorD function as sensors, detecting and/or digesting the phage
486 genome and transferring this signal to the ZorAB channel. First of all, we have shown that the
487 defense is direct and not through abortive infection, refuting a prior hypothesis of ZorAB
488 functioning as a ZorCD–DNA activated pore. Second, ZorC and ZorD alone (without ZorAB)
489 show no protection from phage infection. Third, neither bacterial conjugation nor plasmid
490 transformation can activate Zorya, which would be expected if ZorC and/or ZorD act directly upon
491 foreign DNA. Finally, flagellar stator units function in both Gram-positive and Gram-negative
492 bacteria[15], but Zorya is underrepresented in Gram-positive bacteria. The rare presence of Zorya in
493 Gram-positive bacteria may be due to differences in cell wall architecture and/or phage infection
494 mechanisms that prevent effective Zorya function, rather than a more fundamental difference
495 prohibiting basic ZorAB rotary motor function in these bacteria.

496

497 By directly sensing perturbation of the cell envelope, Zorya would introduce an elegant mechanism
498 that exploits the critical first stages of infection for the activation of downstream defense effectors
499 ZorC and ZorD. Due to the distance between the inner membrane and PG layer exceeding the
500 'reach' of the ZorB PGBDs (**Fig. 3a**), ZorAB complexes would be inactive (not anchored to the
501 PG layer) and free to diffuse laterally, as observed for MotAB complexes before flagellar
502 incorporation[15,25]. Perturbation of the PG layer or local curvature of the inner membrane, which
503 can occur during breaching of the cell envelope by phages[26], would bring the ZorB PGBD closer
504 to the PG layer, allowing binding and subsequent activation of the ZorAB motor (**Fig. 6b, c**). Our
505 model predicts that the 'reach' of the ZorB PGBD should be evolutionarily diversified to adapt to
506 different bacteria cell envelope architectures, which appears to be the case (**Extended Data Fig.**
507 **11**). Conceivably, multiple ZorAB complexes could diffuse to the sites of phage penetration,
508 efficiently responding to the invasion signal, where they can recruit ZorCD. Confinement of ZorC
509 and ZorD activation to the region where phage DNA injection occurs would generate a localized
510 defense response at the sub-cellular level, potentially protecting host DNA from effector activity
511 (ZorC/D) without the need of epigenetic-based self vs. non self-discrimination mechanisms[27].
512 Such local defense also saves energy, as it is only activated when needed, and could allow the
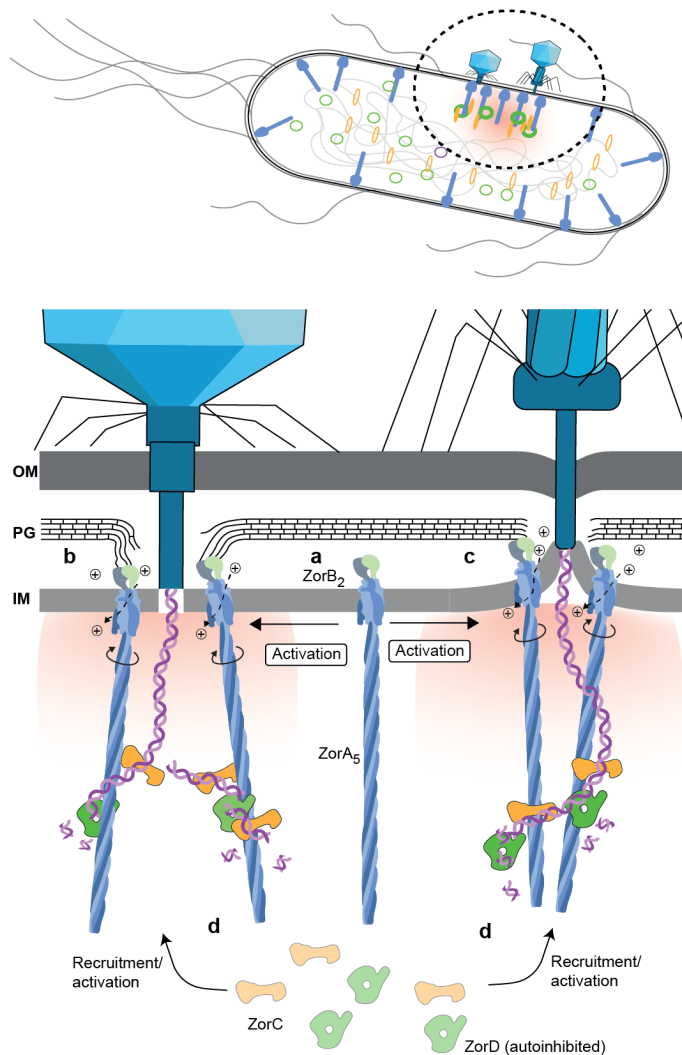513 Zorya system to rapidly turn off again after effective defense.

Figure 6. Proposed model of Zorya activation.
a, An inactive ZorAB complex embedded in the inner membrane. **b-c**, Inactive ZorAB complex detects a signal from phage infection that (**b**) depresses the cell wall or (**c**) induces inner membrane curvature. ZorB PGBDs binds and anchors to the cell wall. Ion translocation through activated ZorAB generates rotational torque, triggering ZorA and its long intracellular tail to rotate around ZorB. **d**, The signal from the ZorAB motor is transferred through the ZorA tail, which recruits and/or activates ZorC and ZorD. Activated ZorC/D binds phage DNA, restricting it to a zone close to the site of phage genome injection, where nuclease degradation of phage DNA prevents phage infection.

In addition to the mechanistic insights directly supported by our data, there are several potential aspects worthy of future investigations. A first open question is the role of two striking features of the ZorAB structure: the rotary motor and the obligatory long tail. One possible explanation for the role of rotation is in signal transduction from phage ingress at the cell envelope to activation of ZorC and ZorD. If the direction of the ZorAB motor is the same as for MotAB (clockwise

530   rotation of A around B, as viewed from the outside of the cell), rotation could potentially induce
531   untwisting of the pentameric ZorA tail super-helix, thereby altering the conformation of the tail to
532   facilitate recruitment or activation of ZorC and/or ZorD (**Extended Data Fig. 12a, b**). A somewhat
533   similar sensory transmission mechanism occurs with bacterial chemosensory arrays and the long
534   ZorA tail might serve to transmit the signal in a manner analogous to the long coiled-coil
535   cytoplasmic signaling domains of methyl-accepting chemotaxis proteins[23]. A second hypothesis
536   that would explain the need for both rotation and a long ZorA tail is that rotation might allow the
537   'reeling in' of the phage DNA around the tail (**Extended Data Fig. 12c**). This would constrain
538   phage DNA to the entry site and keep it in an inactive state (e.g. preventing RNA polymerase
539   access), resolving the time pressure for ZorC and ZorD recruitment and activation, and nuclease
540   activity to take effect before the host takeover mechanisms (see **Extended Data Fig. 12** and
541   **Legend Discussion**). This would also change the required timescale of the defense, giving the host
542   a fighting chance against phages which often have extremely fast lifecycles. Finally, a long,
543   rotating, flexible tail could increase the possibility of catching phage DNA for degradation.
544
545   Another interesting open question is that we observed in our microscopy experiments the increase
546   in Zorya-mNG foci and intensity for cells infected with Bas24, against which *Ec*ZorI shows
547   protection, as well as T4 (**Extended Data Fig. 10e**), against which it does not. This indicates that
548   the system is activated by both phages, in agreement with the hypothesis that the piercing of the
549   cell envelope is the triggering signal. However, we do not yet know why, despite ZorAB activation,
550   phage T4 is not susceptible to *Ec*ZorI defense (**Fig. 1b**), suggesting T4 resists ZorC or ZorD
551   activity, potentially via a T4-encoded anti-Zorya protein. Phage-encoded proteins that inactivate
552   Zorya effectors may be one reason for the existence of multiple Zorya types, each encoding the
553   ZorAB core but with different effectors[7].
554
555   In summary, we provide structural and functional insight into the Zorya defense system and
556   propose that Zorya functions as a direct defense system against a wide range of phages, which acts
557   during the early infection process by initiating a localized response within the proximity of the
558   phage injection site. Our studies reveal a unique activation signal of an anti-phage defense system
559   and pave the way for further studies to understand its detailed mechanism.

Methods

Phylogenetic analysis of Zorya systems

To create the phylogenetic tree shown in **Fig. 1a**, the operons that encode the Zorya (Zor) system types I, II, and III were download from the PADLOC server[8,28]. As ZorA and ZorB are present in all Zorya types, the tree was generated using concatenated ZorA+B sequences. MMseqs2[29] was used to remove the redundancy with the parameters '–min-seq-id 0.90' and '-c 0.8'. The filtered sequences were then aligned using MAFFT[30] with parameters: --maxiterate 1000 –globalpair. The alignment was then trimmed using trimAl[31] with the parameter: -gt 0.25. The phylogenetic tree was constructed using IQ-TREE[32] with the parameters -nstop 500 -bb 2000 -m LG+G4. iTOL[33] was used for tree display and annotation.

Cloning of Zorya defense system and mutagenesis

The DNA of *E. coli* ZorI full operon was amplified from the *E. coli* strain NCTC9026 genome (purchased from the National Collection of Type Cultures, NCTC) with its native promotor and was subcloned into a modified pACYC vector using In-Fusion cloning strategy (In-Fusion® Snap Assembly Master Mix; TaKaRa Cat. # 638947). The DNA of *P. aeruginosa* ZorI full operon was amplified from the *P. aeruginosa* strain DSM24068 genome (DSMZ-German Collection of Microorganisms and Cell Cultures GmbH; Leibniz Institute) and was subcloned into a modified pACYC vector under *E. coli* ZorI native promotor using In-Fusion cloning strategy. For generating mutations (point mutations, deletions, mNeonGreen tag insertion, *Ec*ZorI ZorC or ZorCD genes replaced by *Pa*ZorI ZorC or ZorCD genes), plasmids were constructed based on standard cloning techniques (In-fusion snap assembly (TakaraBio)). All plasmids were verified by either Sanger or nanopore sequencing.

Phage infectivity assays

The host *E. coli* MG1655 ΔRM[19] possessing either pControl (pACYC) or p*Ec*ZorI (or mutants thereof) were grown overnight in LB + Chloramphenicol (Cm; 25 μg/mL). Efficiency of plaquing (EOP) assays were performed using bacterial lawns of the host strain in 0.35% LB agar + 10 mM $MgSO_4$ + 2 mM $CaCl_2$ overlaid onto 1.5% LB agar + Cm. Ten-fold dilution series of phages were spotted onto the overlays, air-dried, then the plates were incubated overnight at 30°C. Liquid culture infection time courses were performed in 96-well plates in an incubated shaking plate reader at 30°C. The time courses were begun with cells at an OD_{600} of 0.05 and phages were added at the indicated MOI, assuming an OD_{600} to cell ratio of 3×10^8 cells per OD_{600} unit.

597

Phage adsorption and one-step growth curves assays

599

600 Overnight cultures of *E. coli* MG1655 ΔRM possessing either pControl or p*Ec*ZorI were used to
601 inoculate fresh LB + Cm cultures at a 1:100 dilution. The inoculated cultures were grown at 30 °C
602 with shaking until reaching an OD_{600} of 0.4–0.6, then harvested by centrifugation, washed with
603 LB + Cm, and resuspended at an OD_{600} of 1.0 in LB + 10 mM $MgSO_4$ + 2 mM $CaCl_2$. For phage
604 the adsorption assays, 10 mL samples of resuspended cells were infected with phage Bas24 at an
605 MOI of 10^{-4}, then the samples were mixed and incubated at 30°C without shaking. For the 0 min
606 timepoint (total input phages), 100 µL samples were removed and added to 0.35% LB Agar seeded
607 with *E. coli* MG1655 ΔRM + pControl (as an indicator lawn), then poured on top of 1.5% LB agar
608 + Cm. For each subsequent time point, 1 mL samples were taken, centrifuged to pellet cells, then
609 the supernatant (containing unabsorbed phages) was filtered through a 0.2 µm PES syringe filter.
610 Samples (100 µL) of the filtered supernatant were added to indicator overlays (as above) poured
611 onto 1.5% LB agar + Cm. All overlay plates were incubated overnight at 30°C before counting
612 plaques. For each timepoint, the percentage of unabsorbed phages was calculated as the timepoint
613 plaque count / plaque count for the time 0 min pControl sample. For the one-step phage growth
614 curves (burst time and size), 2 mL samples of the cells resuspended at and OD_{600} of 1.0 in LB +
615 10 mM $MgSO_4$ + 2 mM $CaCl_2$ (as above) were infected with phage Bas24 at an MOI of MOI of
616 10^{-4}, then the samples were mixed and two 10-fold diluted samples were prepared, then the dilution
617 series for each sample was incubated at 30°C without shaking. At the indicated timepoints, 100
618 µL samples of each dilution were removed and added to 0.35% LB Agar seeded with E. coli
619 MG1655 ΔRM + pControl (as an indicator lawn), then poured on top of 1.5% LB agar + Cm. All
620 overlay plates were incubated overnight at 30°C before counting plaques. For each timepoint, the
621 plaque forming units (PFU) were normalized to the PFU of the 0 min pControl samples.

622

Conjugation assays

624

625 Plasmids encoding kanamycin (Km) resistance and each possessing different origins of
626 replications (ColE1;pMAT16, RSF1010;pPF1825[34], pBBR1;pSEVA237R[35], or RK2;pPF1619)
627 were conjugated from the *E. coli* donor ST18[36,37](auxotroph requiring supplementation with 5-
628 aminolevulinic acid; ALA) into the *E. coli* recipient MG1655 ΔRM possessing either pControl or
629 p*Ec*ZorI. Mattings were performed at the indicated donor to recipient ratios and incubated
630 overnight on LB agar + Cm + ALA at 30 °C. The conjugation efficiency was determined by plating
631 dilution series of the matings onto LB agar + Cm + Km (transconjugants) and LB agar + Cm (total
632 recipients). The transconjugant frequency was defined as the transconjugant CFU/recipient CFU.

633

634   *Transformation assays*

635

636   Chemically competent cells of *E. coli* MG1655 ΔRM possessing either pControl or p*Ec*ZorI were
637   prepared by the Inoue method[38], with HEPES-KOH pH 6.8 used for the transformation buffer.
638   Cells were stored in 200 µL aliquots at -80 °C prior to use. For each transformation assay, 5 ng of
639   plasmid (quantitated using a Qubit BR kit) was used. Plasmids used were as above for the
640   conjugation assays (ColE1;pMAT16, or pBBR1;pSEVA237R).

641

642   *Cell survival assays*

643

644   Overnight cultures of *E. coli* MG1655 ΔRM possessing either pControl or p*Ec*ZorI were used to
645   inoculate fresh LB + Cm cultures at a 1:100 dilution. The inoculated cultures were grown at 30 °C
646   with shaking until reaching an OD_{600} of 0.4–0.6, then harvested by centrifugation, washed with
647   LB + Cm, and resuspended at an OD_{600} of 0.2. Phage Bas24 was then added at an MOI of 5 to
648   each sample; control samples without phage addition were also included. After 20 min adsorption,
649   10-fold serial dilutions of each sample were plated (100 µL each) on LB + Cm, then incubated
650   overnight at 30°C. The cell survival rate was calculated as the CFU obtained + Bas24/CFU
651   obtained without phage addition.

652

653   *Phages and phage genome purification*

654

655   Phage primary stocks were prepared using the double-agar method[39] by setting the grow conditions
656   to almost confluent plaques. The phages were collected by adding SM buffer (100 mM NaCl, 8
657   mM $MgSO_4$, 50 mM Tris-HCl, pH 7.5, 5mM $CaCl_2$) on top of the overly agar and mixed for 4 h
658   at 4 °C. The suspension was collected and centrifuged 15 min at 4000 g. High titer phage samples
659   were obtained by inoculating 1-3 L of LB with a 10^3 dilution of an overnight culture of MG1655
660   ΔRM and grown at 37 °C to and OD_{600} of 0.3. The bacterial culture was inoculated with the primary
661   stock to an MOI of 0.025 and infection was carried out at 37 °C at 90 rpm until a clear lysate was
662   obtained. The lysate was harvested at 4000 g, 15 min and 4 °C. After decanting the supernatant, 1
663   µg/mL of DNase I and 1 µg/mL of boiled RNase A were added to the cleared lysate. The lysate
664   was gently stirred at 90 rpm for 30 min at room temperature (RT).

665

666   Phages were concentrated by polyethylene glycol (PEG) precipitation. NaCl was gradually added
667   to a final concentration of 1 M, followed by gradual addition of 10% PEG 8,000 with continuous
668   stirring at RT until dissolved. After obtaining a clear solution, the lysate was stirred (100 rpm, 30
669   min; 4°C) and left overnight at 4°C. The lysate was centrifuged (15,000 g, 1 h, 4°C) and the clear
670   supernatant was removed. The precipitate was resuspended in the minimal amount (up to 2 ml) of
671   SM buffer that allowed solubilization. Insoluble materials were removed by adding 20% v/v of

672 chloroform and centrifuged (8,000 g, 10 min). The supernatant was stored at 4°C to be used as
673 phage sample for the following step. The phage was then purified by rate zonal separation using
674 OptiPrepTM Density Gradient Medium (Sigma Aldrich) density gradient ranging from 50 to 10%,
675 diluted in SM media. Phage sample was applied on the top of the gradient and centrifuged (150,000
676 g, 18 h, 4°C). The phage was extracted, dialyzed against SM buffer and samples were stored at
677 4°C. The phage genomes were extracted using the Phage DNA isolation kit from Norgen Biotek,
678 aliquoted and stored at -20°C.

679

680 *Protein expression and purification*

681

682 ZorAB
683 The full-length genes of *E. coli* ZorA and ZorB code for 729 and 246 residues, respectively. The
684 tandem gene was PCR amplified from the *E. coli* strain NCTC9026 genome (purchased from the
685 National Collection of Type Cultures, NCTC) and subcloned into a modified pET vector
686 containing a C-terminal human rhinovirus (HRV) 3C protease cleavage site and a twin-Strep-tag
687 II (resulting in pET11a-ZorA-ZorB-3C-TSII). The plasmids containing the recombinant genes
688 were transfected into *E. coli* C43(DE3) competent cells and the proteins were expressed in LB
689 medium. When the culture OD reached to 0.6-0.8, the temperature was decreased from 37°C to
690 24°C (OD reached approximately 0.8-1.0), and 0.5 mM isopropyl β-D-1-thiogalactopyranoside
691 (IPTG) was added for overnight protein induction. The culture was harvested, and the cell pellet
692 was resuspended in buffer A containing 20 mM HEPES-NaOH pH 7.5, 300 mM NaCl
693 supplemented with EDTA-free protease inhibitor (Thermo Fisher Scientific) and lysozyme from
694 chicken white egg (Sigma) to a final concentration of 50 μg/mL and Deoxyribonuclease I from
695 bovine (Sigma) to a final concentration of 30 μg/mL. The mixture was disrupted by high-pressure
696 homogenizer and spun at 185,000 g for 1 h. The pellet containing the membrane was collected and
697 was solubilized using buffer B containing 30 mM HEPES-NaOH pH7.5, 300 mM NaCl, 10%
698 glycerol, 2% Lauryl Maltose Neopentyl Glycol (LMNG; Anatrace), supplemented with EDTA-
699 free protease inhibitor at 4°C for 2 h. The solubilized membrane was then spun at 90,000 g rpm
700 for 40 min and the supernatant was loaded onto a gravity flow column containing 2 mL (resin
701 volume) of Strep-Tactin® Superflow® high-capacity resin (IBA), pre-equilibrated with wash
702 buffer containing 20 mM HEPES-NaOH pH 7.5, 300 mM NaCl, 10% glycerol and 0.005% LMNG.
703 The resins were washed five times with 2-3 resin volumes of the wash buffer and elution was
704 carried out five times with 0.5 resin volume (1 mL) of elution buffer containing 20 mM HEPES-
705 NaOH pH 7.5, 300 mM NaCl, 10% glycerol, 0.005% LMNG and 10 mM desthiobiotin). The
706 recombinant protein was then concentrated and loaded onto a pre-equilibrated (20 mM HEPES-
707 NaOH pH 7.5, 150 mM NaCl, 0.002% LMNG) Superose 6 Increase 10/300 GL Size-exclusion
708 chromatography column. Fractions from the elution peak corresponding to the molecular weight
709 of ZorAB complex were pooled, and the protein was concentrated for cryo-EM grids preparation

710 and functional experiments. The procedures of expression and purification of ZorAB mutants were
711 similar as the ZorAB wild type.

712

713 ZorC
714 The predicted ZorC gene codes for 560 residues. The ZorC gene together with a short region
715 upstream of ZorC N-terminus that codes for 7 residues (LPVGYAT) was PCR amplified from the
716 DNA genome of *E. coli* strain NCTC9026 and subcloned into the modified pET vector (resulting
717 in pET11a-ZorC-3C-TSII). *E. coli* BL21 (DE3) gold chemically competent cells were transformed
718 with the plasmids and the protein was expressed in LB medium with the presence of 100 μg/mL
719 of ampicillin. Briefly, when the OD reached to 1.0-1.2, decreased the temperature to 16°C and 0.5
720 mM isopropyl β-D-1-thiogalactopyranoside (IPTG) was added for overnight protein induction.
721 The culture was harvested, and the cell pellet was resuspended using buffer containing 20 mM
722 Tris pH 7.5, 10% glycerol and 500 mM NaCl supplemented with EDTA-free protease inhibitor
723 (Thermo Fisher Scientific). The cells were lysed using an Avestin Emulsiflex C3 homogeniser,
724 cooled to 4°C, and spun at 18,000 g for 40 minutes. The supernatant was then added to a gravity
725 flow column containing 3 mL (resin volume) of Strep-Tactin® Superflow® high-capacity resins
726 (IBA), pre-equilibrated with wash buffer (20 mM Tris pH 7.5, 10% glycerol and 500 mM NaCl).
727 Resins were washed five times with 2-3 resin volumes of wash buffer and elution was performed
728 with 4 CV of elution buffer (20 mM Tris-HCl pH 7.5, 500 mM NaCl and 10 mM desthiobiotin).
729 The recombinant protein was pooled and concentrated and was loaded onto a pre-equilibrated (20
730 mM Tris-HCl pH 7.5, 500 mM NaCl) Superose 6 Increase 10/300 GL Size exclusion
731 chromatography column. Peak fractions were pooled, and another round of size exclusion
732 chromatography was carried out with buffer 20 mM HEPES-NaOH pH 7.5, and 150 mM NaCl to
733 decrease NaCl concentration. Fractions from the elution peak corresponding to the molecular
734 weight of ZorC were pooled and the protein was concentrated to approximately 1 mg/mL for cryo-
735 EM grids preparation and functional experiments. ZorC proteins used for electromobility shift
736 assays (EMSAs) was kept in elution buffer B (20 mM Tris-HCL pH 7.5, 500 mM NaCl, 10 %
737 glycerol) and flash frozen in small aliquots and stored at -80C until use. Sample purity was
738 assessed by SDS-PAGE. The procedures of expression and purification of ZorC mutants were
739 similar to those for the ZorC wild type.

740

741 ZorD
742 The predicted ZorD gene coding 1,086 residues was PCR amplified from the DNA genome of *E.*
743 *coli* strain NCTC9026 and was subcloned into the modified pET vector. The expression and
744 purification of ZorD protein were similar to ZorC protein, except for the purification buffer.
745 Briefly, the suspension buffer contained 150 mM NaCl and 20 mM HEPES at pH 7.5, 10 glycerol;
746 the wash buffer was the same as the suspension buffer and the elution buffer contained 150 mM
747 NaCl and 20 mM HEPES-NaOH at pH 7.5, 10% glycerol with 10 mM desthiobiotin; and the size
748 exclusion chromatographic buffer contained 20 mM HEPES-NaOH pH 7.5 and 150 mM NaCl.
749 Purified ZorD was concentrated to 0.4-0.6 mg/mL for functional experiments and cryo-EM grids

750 preparation. For nuclease experiment, ZorD protein was kept in the elution buffer and flash frozen
751 in small aliquots and stored at -80°C until use.
752

753 *Cryo-EM grid preparation, data collection, model building, and refinement.*
754

755 ZorAB
756 Freshly purified ZorAB sample was concentrated to 2-3 mg/mL and 2.7 μL protein was applied
757 onto the glow-discharged (30 s, 5 mA) grids (Quantifoil R0.6/1 300 mesh Au) and plunge-frozen
758 into liquid ethane using a Vitrobot Mark IV (FEI, Thermo Fisher Scientific), with the settings: 100%
759 humidity, 4ºC, blotting force 25, 4-6 s blot time and 7 s wait time; Movies were collected using
760 the semi-automated acquisition program EPU (FEI, Thermo Fisher Scientific) on a Titan Krios G2
761 microscope operated at 300 keV paired with a Falcon 3EC direct electron detector (FEI, Thermo
762 Fisher Scientific). Images were recorded in electron counting mode, at 96,000x magnification with
763 a calibrated pixel size of 0.832 Å and an underfocus range of 0.7 to 2.5 μm. The number of
764 micrographs and total exposure values for the different datasets are summarized in Table S1. Grids
765 preparation, and data collection strategies of the ZorAB mutants were similar to those for the
766 ZorAB wild type.
767

768 ZorC
769 Purified ZorC (3 μL at ~1 mg/mL) was applied onto glow-discharged (30 s, 5 mA) grids
770 (UltrAuFoil R 0.6/1, 300 mesh, Gold) and plunge-frozen into liquid ethane using a Vitrobot Mark
771 IV (FEI, Thermo Fisher Scientific), with the settings: 100% humidity, 4 ºC, blotting force 20, 4 s
772 blot time and 10 s wait time; Movies were collected using the semi-automated acquisition program
773 EPU (FEI, Thermo Fisher Scientific) on a Titan Krios G2 microscope operated at 300 keV paired
774 with a Falcon 3EC direct electron detector (FEI, Thermo Fisher Scientific). Images were recorded
775 in electron counting mode, at 96,000x magnification with a calibrated pixel size of 0.832 Å and an
776 underfocus range of 1 to 2.5 μm. The number of micrographs and total exposure values for the
777 datasets are summarized in **Extended Data Table 1**.
778

779 ZorD
780 ZorD showed preferred orientation of particles on ice. 0.5% zwitterionic detergent CHAPSO
781 (Anatrace) was added to the purified sample to a final concentration of 0.0125% before cryo-EM
782 grid preparation. For the apo form, the preparation of grids was similar to ZorC. For ZorD in
783 complex with ATP-γ-S, 4 μL of 0.1 mM ATP-γ-S was added into 400 μL of purified ZorD at
784 0.0375 mg/ml. The mixture was concentrated to 15 μL to reach a ZorD concentration of around
785 0.6 mg/mL. The grid preparation was similar to ZorC. The number of micrographs and total
786 exposure values for the different datasets are summarized in **Extended Data Table 1**.
787

788 *Cryo-EM data processing*

789

790 All datasets were processed using cryoSPARC[40] v4.2.1, unless otherwise stated. We started by
791 using Patch motion correction to estimate and correct for full-frame motion and sample
792 deformation (local motion). Patch Contrast function (CTF) estimation was used to fit local CTF to
793 micrographs. Micrographs were manually curated to remove the relatively ice thickness value
794 bigger than 1.1 and the CTF value worse than 3.5 Å. We performed particle picking by template
795 picking or using topaz particle picking[41]. Particles were extracted with a box size of 500 pixels for
796 ZorAB datasets, 256 pixels for the ZorC dataset, and 400 pixels for the ZorD dataset. One round
797 of 2D classification was performed followed by *ab initio* reconstruction. Heterogeneous
798 refinement was used to exclude broken particles. Non-uniform refinement was applied with a
799 dynamic mask to obtain a high-resolution map. Local refinement was additionally performed with
800 a soft mask to achieve a higher-resolution map of some flexible regions. For all datasets, the
801 number of movies, the number of particles used for the final refinement, map resolution, and other
802 values during data processing are summarized in the **Extended Data Table 1**.

803

804 *Model building and validation*

805

806 We used AlphaFold2[42] (AF2) to predict all the initial models. The predicted models were manually
807 fit into the cryo-EM density by using UCSF ChimeraX[43]. The model was refined in Coot[44] or
808 refined using StarMap[45] in the case of ZorC, for which the map is anisotropic and the resolution is
809 modest. The model was then refined against the map using PHENIX real space refinement[46]. The
810 ZorAB composite model was constructed by extending the pentameric tail as an idealized right-
811 handed super-helical coiled coil. Local conformations were manually adjusted in PyMol[47](v2.5)
812 and optimized through energy minimization using Gromacs (v2022.5)[48]. However, it's worth
813 noting an irregularity in the AF2 model, specifically in residues 312 to 322, which introduces a
814 significant twist in the tail, raising possibilities of other pentameric forms of the ZorA tail and
815 further reflecting its conformational dynamics.

816

817 *Peptidoglycan (PG) purification and pull-down experiment*

818

819 Peptidoglycan was purified from *E. coli* strain MG1665 ΔRM with the protocol adapted from[49]
820 Briefly, *E. coli* strain MG1665 ΔRM cells were incubated in 1 L LB media until the $OD_{600\ nm}$
821 reached 0.8. Cells were harvested and resuspended in 12 mL PBS buffer and split into two 50 mL
822 falcon tubes, SDS solution was added to final the concentration of 6%. The falcon tubes were
823 boiled for 1 hour while stirred at 500 rpm. The heat was turned off and the tube was allowed to
824 cool to ambient temperature overnight. The next day, the solutions from both Falcon tubes were
825 pooled into one 50 mL Falcon tube, and centrifuged at room temperature for 45 mins at 108,000
826 g. The pellet was washed five times with 5 mL Milli-Q® water. The PG was resuspended in 20

827 mL of buffer containing 50 mM Tris-HCl, pH 7.0, and α-amylase was added (SigmaAldrich) to a
828 final concentration of 100 μg/mL and incubated for 2 hours at 37°C. Next, 50 μg/mL RNase A
829 (Roche) and 10 μg/mL DNase (Sigma-Aldrich) were added and incubated for an additional 2 hours
830 at 37°C. Then, the mixture was supplemented with 20 mM $MgSO_4$, 10 mM $CaCl_2$, and 100 μg/mL
831 trypsin (SigmaAldrich), and incubated at 37°C overnight. The following day, EDTA at pH 8 was
832 added to a final concentration of 10 mM to the mixture and SDS solution to a final concentration
833 of 1%. The mixture was boiled for 20 mins in a water bath and allowed to cool to ambient
834 temperature. The tube was centrifuged at 108,000 g for 45 minutes. The resulting pellet was
835 washed five times with Milli-Q® water to remove residual SDS. Finally, the pellet was
836 resuspended in 300 μL of Milli-Q® water, aliquoted into 35 μL portions, and stored at -20 °C. For
837 PG pull-down assays, the PG was washed with 1 mL PBS+0.002% LMNG buffer and centrifuged
838 at 20,000 g for 30 minutes. 10 μL of purified ZorAB was incubated (at a concentration of 2 mg/mL)
839 with the PG at room temperature for 1 hour, then centrifuged at 20,000 g for 30 minutes, the
840 supernatant was retained for SDS gel analysis. The pellet was resuspended with 20 μL of buffer
841 and 5 μL of loading dye was added for SDS gel analysis.
842

843 *ZorC DNA-binding experiments*

844

845 *Electromobility shift assays:*

846

847 Frozen aliquots of ZorC and ZorC mutants in Elution buffer B (20 mM Tris-HCL pH 7.5, 500 mM
848 NaCl, 10% glycerol) were thawed, and centrifuged to remove aggregates and diluted to 2 μM in
849 phosphate-buffer saline (PBS) (15.2 mM $NaHPO_4$, 0.90 mM calcium chloride, 2.7 mM potassium
850 chloride, 1.47 mM potassium dihydrogen phosphate, 8.1 mM sodium hydrogen phosphate, 0.49
851 mM magnesium chloride, 137.9 mM sodium chloride at pH 6.8). Scrambled dsDNA substrates
852 (5'-FAM-CTAGAAAGACTTTTAACAGTGGCCTTATTAAATGACTT
853 CTCAACCATCTTGCTGA-3') were incubated with a protein in PBS. All components were
854 incubated at 4°C for 10 min. Glycerol was added to the reactions prior to loading on a 2% DNA
855 agarose gel. Samples were run for 15-25 minutes at 250 V, and the gels were visualized using
856 Odyssey® XF Imaging System at wavelength 600 nm.

857

858 *Nuclease assays*

859

860 ZorD was incubated with 200 ng pUC19 (linearized by KpnI (NEB) enzyme) in the reaction buffer
861 containing 1 × Cutsmart buffer (NEB), 2 mM ATP (NEB) in a total volume of 25 μl. Mixture was
862 incubated at 37°C for 1 hour and shaken at 600 rpm using an Eppendorf ThermoMixer. DNA
863 product was purified using a NucleoSpin Gel and PCR Clean-up kit (Machery Nagel) using the
864 standard protocol and was analyzed with 1% E-Gel™ EX. For the reaction with the phage genomes,
865 200 nM Proteins were incubated with around 100 ng purified phage genomic DNA in the same

866 reaction buffer indicated above. The reactions were terminated by adding 1× E-gel loading buffer
867 and product was analyzed with 1% E-Gel™ EX.
868

869 *Mass spectrometry sample preparation*

870

871 Overnight cultures *of E. coli* MG1665 ΔRM, transformed with plasmids encoding the Zorya
872 operon (or control), were used to inoculate (at a 1:1000 dilution) 3 mL LB media with antibiotics,
873 then grown to an OD_{600} of approximately 0.4. The cell pellet was collected, resuspended in 500
874 μL of 0.2 M Tris-HCl pH 8.0, and incubated for 20 min. 250 μL of buffer containing 0.2M Tris-
875 HCl pH 8.0, 1 M sucrose, and 1 mM EDTA, was added into the solution along with 3 μL of 10
876 mg/mL lysozyme. The mixture was incubated for 30 minutes, and 250 μL of 6% SDS was added
877 to a final concentration of 1%, after which the sample was heated to 99°C for 10 min. The mixture
878 was sonicated to fragment DNA and RNA.

879

880 For MS analysis, we performed Protein Aggregate Capture digestion of proteins[50]. To this end,
881 250 μL of bacterial lysate was taken from the total sample, and 750 μL of acetonitrile was added
882 into the mixture, along with 50 μL magnetic microspheres that had been prewashed with PBS
883 buffer. The mixture was allowed to settle for 10 min, prior to retention of the magnetic
884 microspheres by magnetic plate. Beads were washed once with 1 mL acetonitrile, and once with 1
885 mL of 70% ethanol, after which all ethanol was removed and beads were stored at −20°C until
886 further processing. Frozen beads were thawed on ice, supplemented with 100 μL ice-cold 50 mM
887 Tris-HCl pH 8.5 buffer supplemented with 2.5 ng/μL Lys-C, and gently mixed (on ice) every 5
888 min for 30 min. Digestion was performed for 3 h using a Eppendorf ThermoMixer shaking at 1,250
889 rpm at 37 °C. Following this, beads were chilled on ice, and 250 ng of sequencing-grade trypsin
890 was added, after which samples were gently mixed (on ice) every 5 min for 30 min. Final digestion
891 was performed overnight using a Eppendorf ThermoMixer shaking at 1,250 rpm at 37°C. Peptides
892 were separated from magnetic microspheres using 0.45 μm filter spin columns, and peptides were
893 reduced and alkylated by adding TCEP and chloroacetamide to 5 mM for 30 min prior to peptide
894 clean-up via low-pH C18 StageTip procedure. C18 StageTips were prepared in-house, by layering
895 four plugs of C18 material (Sigma-Aldrich, Empore SPE Disks, C18, 47 mm) per StageTip.
896 Activation of StageTips was performed with 100 μL 100% methanol, followed by equilibration
897 using 100 μL 80% acetonitrile (ACN) in 0.1% formic acid, and two washes with 100 μL 0.1%
898 formic acid. Samples were acidified to pH <3 by addition of trifluoroacetic acid to a concentration
899 of 1%, after which they were loaded on StageTips. Subsequently, StageTips were washed twice
900 using 100 μL 0.1% formic acid, after which peptides were eluted using 80 μL 30% ACN in 0.1%
901 formic acid. All fractions were dried to completion using a SpeedVac at 60 °C. Dried peptides
902 were dissolved in 25 μL 0.1% formic acid (FA) and stored at −20 °C until analysis using mass
903 spectrometry (MS).

904

905   Approximately 1 μg of peptide was analyzed per injection. All samples were analyzed on an
906   EASY-nLC 1200 system (Thermo Fisher Scientific) coupled to an Orbitrap™ Astral™ mass
907   spectrometer (Thermo Fisher Scientific). Samples were analyzed on 20 cm long analytical columns,
908   with an internal diameter of 75 μm, and packed in-house using ReproSil-Pur 120 C18-AQ 1.9 μm
909   beads (Dr. Maisch). The analytical column was heated to 40 °C, and elution of peptides from the
910   column was achieved by application of gradients with stationary phase Buffer A (0.1% FA) and
911   increasing amounts of mobile phase Buffer B (80% ACN in 0.1% FA). The primary analytical
912   gradient ranged from 10 %B to 38 %B over 57.5 min, followed by a further increase to 48 %B
913   over 5 min to elute any remaining peptides, and by a washing block of 15 min. Ionization was
914   achieved using a NanoSpray Flex NG ion source (Thermo Fisher Scientific), with spray voltage
915   set at 2 kV, ion transfer tube temperature to 275 °C, and RF funnel level to 50%. All full precursor
916   (MS1) scans were acquired using the Orbitrap™ mass analyzer, while all tandem fragment (MS2)
917   scans acquired in parallel using the Astral™ mass analyzer. Full scan range was set to 300-1,300
918   m/z, MS1 resolution to 120,000, MS1 AGC target to "250" (2,500,000 charges), and MS1
919   maximum injection time to "150". Precursors were analyzed in data-dependent acquisition (DDA)
920   mode, with charges 2-6 selected for fragmentation using an isolation width of 1.3 m/z and
921   fragmented using higher-energy collision disassociation (HCD) with normalized collision energy
922   of 25. Monoisotopic Precursor Selection (MIPS) was enabled in "Peptide" mode. Repeated
923   sequencing of precursors was minimized by setting expected peak width to 20 s, and dynamic
924   exclusion duration to 20 s, with an exclusion mass tolerance of 10 ppm and exclusion of isotopes.
925   MS2 scans were acquired using the Astral mass analyzer. MS2 fragment scan range was set to
926   100-1,500 m/z, MS2 AGC target to "50" (5,000 charges), MS2 intensity threshold to 50,000
927   charges per second, and MS2 maximum injection time to 5 ms; thus requiring a minimum of 250
928   charges for attempted isolation and identification of each precursor. Duty cycle was fixed at 0.3 s,
929   acquiring full MS scans at ~3.3 Hz and with auto-fitting of Astral scans resulting in MS2
930   acquisition at a rate of ~100-200 Hz.

931

932   *Mass spectrometry data analysis*

933

934   All RAW files were analyzed using MaxQuant software (v2.4.3.0)[51], the earliest release version
935   to support Astral RAW files. Default MaxQuant settings were used, with exceptions outlined
936   below. For generation of the in silico spectral library, the four full-length Zorya protein sequences
937   were entered into a FASTA database, along with all (23,259) Swiss-Prot-reviewed *E. coli*
938   sequences (taxonomy identifier 562) downloaded from UniProt[52] on the 7th of September, 2023.
939   The data was first searched using pFind (v3.2.0)[53] , using the "Open Search" feature to determine
940   overall peptide properties and commonly occurring (affecting >1% of PSMs) peptide modification
941   in an unbiased manner. For searching Astral .RAW files using pFind, .RAW files were first
942   converted to .mzML using OpenMS (v3.0.0)[54]. For the main data search using MaxQuant,
943   digestion was performed using "Trypsin/P" with up to 2 missed cleavages (default), with a
944   minimum peptide length of 6 and a maximum peptide mass of 5,000 Da. No variable modifications

945   were considered for the first MS/MS search, which is only used for precursor mass recalibration.
946   For the MS/MS main search a maximum allowance of 3 variable modifications per peptide was
947   set, including protein N-terminal acetylation (default), oxidation of methionine (default),
948   deamidation of asparagine, peptide N-terminal glutamine to pyroglutamate, and replacement of
949   three protons by iron (cation Fe[III]) on aspartate and glutamate. Unmodified and modified
950   peptides were stringently filtered by setting a minimum score of 10 and 20, and a minimum delta
951   score of 20 and 40, respectively. First search mass tolerance was set to 10 ppm, and maximum
952   charge state of considered precursors to 6. Label-free quantification (LFQ) was enabled, "Fast
953   LFQ" was disabled. iBAQ was enabled. Matching between runs was enabled with a match time
954   window of 1 min and an alignment time window of 20 min. Matching was only allowed between
955   same-condition replicates. Data was filtered by posterior error probability to achieve a false
956   discovery rate of <1% (default), at the peptide-spectrum match, protein assignment, and site-decoy
957   levels.
958

959   *Mass spectrometry data statistics*

960

961   All statistical data handling was performed using the Perseus software[55], including data filtering,
962   log2-transformation, imputation of missing values (down shift 1.8 and width 0.15), and two-tailed
963   two-sample Student's t-testing with permutation-based false discovery rate control. In order to
964   determine relative concentration of all proteins in the samples, LFQ-normalized intensity values
965   for each protein were adjusted by molecular weight. To approximate absolute copy-numbers, we
966   extracted known protein copy-numbers based on the "LB" condition as reported by Schmidt et
967   al.,[56] log2-transformed them, and aligned them to the molecular-weight adjusted LFQ intensity
968   values from our own data, resulting in 1,901 out of 2,418 quantified protein-groups receiving a
969   known copy-number value ($R^2 = 0.6129$). Next, we subtracted the overall median from all log2
970   values, and determined the absolute delta between the values of each pair. Out of all pairs, 459 had
971   a log2 delta of <0.5, which we considered as a "proteomic ruler". Linear regression was performed
972   on the remaining pairs ($R^2 = 0.9868$) to determine a conversion factor between MW-adjusted LFQ
973   intensity and absolute copy-number.

974

975   *TIRF microscopy cultivation conditions*

976

977   Overnight cultures of *E. coli* strains expressing ZorB, C or D translational fusions to mNeongreen
978   were incubated shaking at 180 rpm in LB Lennox containing 20 mM $MgSO_4$, 5 mM $CaCl_2$ and
979   supplemented with 12.5 µg/ml chloramphenicol at 30 °C. On the next day, a sub-culture was
980   inoculated 1:100 and grown at 30 °C until an OD600 between 0.3-0.5 was reached. Subsequently,
981   cells were diluted to an OD600 of 0.2 to ensure reproducible ratios between bacteria and phages.
982   Cells were then exposed to phages at indicated MOIs or incubated untreated for 30 min in a 2 mL
983   Eppendorf tube under shaking conditions (<650 rpm in an Eppendorf ThermoMixer). For TIRF

984 microscopy, 1 µl of cells and phage mix was spotted on an agarose pad (1.2% in MQ of
985 UltraPure™ Agarose, Invitrogen) and directly imaged.
986

987 *TIRF microscopy acquisition and data evaluation*

988

989 TIRF microscopy was performed using a Nikon Eclipse Ti2 inverted microscope equipped with
990 an ILAS 2 TIRF module (Gataca Systems) and a TIRF 100x/1.49 oil objective. Samples were
991 excited at 50 ms exposure for 14 frames using a 488 nm laser (200 mW) at 80% and emission was
992 recovered via a quad TRIF filter cube (emission: 502-549 nm). The second frame in the fluorescent
993 channel of the acquired TIRF microscopy images was denoised using the Nikon software package
994 Denoise.ai. Subsequently, fluorescent maxima of ZorB, C or D translational fusions to
995 mNeongreen were detected using MicrobeJ[57] run in Fiji[58]. Statistics were calculated in Prism
996 GraphPad 9[59] by applying the in-built analyses of unpaired t-tests or one-way ANOVA.

997

998 *Bioinformatic analyses of ZorA motor and tail lengths*

999

1000 PADLOC v1.1.0[8,28] with PADLOC-DB v1.4.0 was used to identify Zorya systems in RefSeq
1001 v209[60] bacterial and archaeal genomes. Of the systems identified, we excluded those containing
1002 pseudogenes or more than one copy of each Zorya gene, or systems with non-canonical gene
1003 arrangements (Zorya genes are typically on the same strand, in type-specific conserved gene orders,
1004 e.g. ZorABCD, ZorABE, or ZorGABF for types I–III, respectively). To reduce redundancy due to
1005 highly related genome sequences in the RefSeq database, we then selected representative Zorya
1006 systems by clustering the sequences (using MMseqs2 v14.7e284[29] with options: --min-seq-id 0.3
1007 --coverage 0.8) of the proteins encoded by the three adjacent open reading frames on either side
1008 of each Zorya system, then randomly selected one system for each distinct set of these flanking
1009 genes (i.e. unique genetic context of the Zorya system). The ZorA and ZorB sequences from the
1010 representative Zorya systems were then clustered using MMseqs2 with options: --min-seq-id 0.3 -
1011 -coverage 0.95. Structures were predicted for one representative of each ZorA and ZorB cluster
1012 using ColabFold v1.5.2[42,61,62] with options: --num-recycle 3 --num-models 1 --model-type auto --
1013 amber --use-gpu-relax. Structures predictions were run as $ZorA_5ZorB_2$ multimers. The resulting
1014 structures were inspected manually (using PyMOL v2.5.4[47]) to identify the start of the ZorA tail.
1015 The rest of the sequences in each cluster were aligned to the representative sequence using
1016 MUSCLE v5.1[63] using the Parallel Perturbed ProbCons algorithm (default) or the Super5
1017 algorithm if the cluster contained more than 100 sequences. The start of the tail for the
1018 representative was used to infer the start of the tail for each other protein in the respective
1019 alignment.

1020

1021   *Figure preparation*

1022

1023   Structural figures were prepared using ChimeraX[43], PyMOL[47], Prism GraphPad9 or GraphPad

1024   Prisim10[59] and Adobe Illustrator[64]. The ion permeation pathway show in ZorAB was analyzed

1025   using MOLEonline[65]. The Hydrophobicity and polarity of the ZorAB tail was calculated using

1026   MOLEonline[65]. The electrostatic potential maps were calculated using the APBS[66] electrostatic

1027   Plugin integrated inside Pymol.

1028

1029

References:

1. Labrie, S. J., Samson, J. E. & Moineau, S. Bacteriophage resistance mechanisms. *Nat. Rev. Microbiol.* **8**, 317–327 (2010).

2. Hampton, H. G., Watson, B. N. J. & Fineran, P. C. The arms race between bacteria and their phage foes. *Nature* **577**, 327–336 (2020).

3. Stern, A. & Sorek, R. The phage-host arms race: Shaping the evolution of microbes. *BioEssays* **33**, 43–51 (2011).

4. Smith, W. P. J., Wucher, B. R., Nadell, C. D. & Foster, K. R. Bacterial defences: mechanisms, evolution and antimicrobial resistance. *Nat. Rev. Microbiol.* **21**, 519–534 (2023).

5. Bernheim, A. & Sorek, R. The pan-immune system of bacteria: antiviral defence as a community resource. *Nat. Rev. Microbiol.* **18**, 113–119 (2020).

6. Wang, J. Y. & Doudna, J. A. CRISPR technology: A decade of genome editing is only the beginning. *Science* **379**, eadd8643 (2023).

7. Doron, S. *et al.* Systematic discovery of antiphage defense systems in the microbial pangenome. *Science* **359**, (2018).

8. Payne, L. J. *et al.* Identification and classification of antiviral defence systems in bacteria and archaea with PADLOC reveals new system types. *Nucleic Acids Res.* **49**, 10868–10878 (2021).

9. Gao, L. *et al.* Diverse enzymatic activities mediate antiviral immunity in prokaryotes. *Science* **369**, 1077–1084 (2020).

10. Millman, A. *et al.* An expanded arsenal of immune systems that protect bacteria from phages. *Cell Host Microbe* (2022) doi:10.1016/j.chom.2022.09.017.

11. Stokar-Avihail, A. *et al.* Discovery of phage determinants that confer sensitivity to bacterial immune systems. *Cell* **186**, 1863-1876.e16 (2023).

12. Gao, L. A. *et al.* Prokaryotic innate immunity through pattern recognition of conserved viral proteins. *Science* **377**, eabm4096 (2022).

13. Santiveri, M. *et al.* Structure and Function of Stator Units of the Bacterial Flagellar Motor. *Cell* (2020) doi:10.1016/j.cell.2020.08.016.

14. Deme, J. C. *et al.* Structures of the stator complex that drives rotation of the bacterial flagellum. *Nat. Microbiol.* **5**, 1553–1564 (2020).

15. Hu, H. *et al.* Structural basis of torque generation in the bi-directional bacterial flagellar motor. *Trends Biochem. Sci.* **0**, (2021).

16. Hu, H. *et al.* Ion selectivity and rotor coupling of the Vibrio flagellar sodium-driven stator unit. *Nat. Commun.* **14**, 4411 (2023).

17. Georjon, H. & Bernheim, A. The highly diverse antiphage defence systems of bacteria. *Nat. Rev. Microbiol.* (2023) doi:10.1038/s41579-023-00934-x.

18. Rousset, F. & Sorek, R. The evolutionary success of regulated cell death in bacterial immunity. *Curr. Opin. Microbiol.* **74**, 102312 (2023).

19. Maffei, E. *et al.* Systematic exploration of Escherichia coli phage–host interactions with the BASEL phage collection. *PLOS Biol.* **19**, e3001424 (2021).

20. Roujeinikova, A. Crystal structure of the cell wall anchor domain of MotB, a stator component of the bacterial flagellar motor: Implications for peptidoglycan recognition. *Proc. Natl. Acad. Sci.* **105**, 10348–10353 (2008).

21. Zhu, S. *et al.* Conformational change in the periplamic region of the flagellar stator coupled with the assembly around the rotor. *Proc. Natl. Acad. Sci.* **111**, 13523–13528 (2014).

22. Krapp, L. F., Abriata, L. A., Cortés Rodriguez, F. & Dal Peraro, M. PeSTo: parameter-free geometric deep learning for accurate prediction of protein binding interfaces. *Nat. Commun.* **14**, 2175 (2023).

23. Riechmann, C. & Zhang, P. Recent structural advances in bacterial chemotaxis signalling. *Curr. Opin. Struct. Biol.* **79**, 102565 (2023).

24. Dürr, H., Flaus, A., Owen-Hughes, T. & Hopfner, K.-P. Snf2 family ATPases and DExx box helicases: differences and unifying concepts from high-resolution crystal structures. *Nucleic Acids Res.* **34**, 4160–4167 (2006).

25. Wadhwa, N. & Berg, H. C. Bacterial motility: machinery and mechanisms. *Nat. Rev. Microbiol.* 1–13 (2021) doi:10.1038/s41579-021-00626-4.

26. B, H., W, M., Ij, M. & J, L. Structural remodeling of bacteriophage T4 and host membranes during infection initiation. *Proc. Natl. Acad. Sci. U. S. A.* **112**, (2015).

27. Samson, J. E., Magadán, A. H., Sabri, M. & Moineau, S. Revenge of the phages: defeating bacterial defences. *Nat. Rev. Microbiol.* **11**, 675–687 (2013).

28. Payne, L. J. *et al.* PADLOC: a web server for the identification of antiviral defence systems in microbial genomes. *Nucleic Acids Res.* **50**, W541–W550 (2022).

29. Steinegger, M. & Söding, J. MMseqs2 enables sensitive protein sequence searching for the analysis of massive data sets. *Nat. Biotechnol.* **35**, 1026–1028 (2017).

30. Katoh, K., Rozewicki, J. & Yamada, K. D. MAFFT online service: multiple sequence alignment, interactive sequence choice and visualization. *Brief. Bioinform.* **20**, 1160–1166 (2019).

31. Capella-Gutiérrez, S., Silla-Martínez, J. M. & Gabaldón, T. trimAl: a tool for automated alignment trimming in large-scale phylogenetic analyses. *Bioinformatics* **25**, 1972–1973 (2009).

32. Nguyen, L.-T., Schmidt, H. A., von Haeseler, A. & Minh, B. Q. IQ-TREE: A Fast and Effective Stochastic Algorithm for Estimating Maximum-Likelihood Phylogenies. *Mol. Biol. Evol.* **32**, 268–274 (2015).

33. Letunic, I. & Bork, P. Interactive Tree Of Life (iTOL) v5: an online tool for phylogenetic tree display and annotation. *Nucleic Acids Res.* **49**, W293–W296 (2021).

34. McBride, T. M. *et al.* Diverse CRISPR-Cas Complexes Require Independent Translation of Small and Large Subunits from a Single Gene. *Mol. Cell* **80**, 971-979.e7 (2020).

35. Martínez-García, E. *et al.* SEVA 4.0: an update of the Standard European Vector Architecture database for advanced analysis and programming of bacterial phenotypes. *Nucleic Acids Res.* **51**, D1558–D1567 (2023).

36. Thoma, S. & Schobert, M. An improved Escherichia coli donor strain for diparental mating. *FEMS Microbiol. Lett.* **294**, 127–132 (2009).

37. Jackson, S. A., Fellows, B. J. & Fineran, P. C. Complete Genome Sequences of the Escherichia coli Donor Strains ST18 and MFDpir. *Microbiol. Resour. Announc.* **9**, 10.1128/mra.01014-20 (2020).

38. Inoue, H., Nojima, H. & Okayama, H. High efficiency transformation of Escherichia coli with plasmids. *Gene* **96**, 23–28 (1990).

39. *Bacteriophages*. vol. 501 (Humana Press, 2009).

40. Punjani, A., Rubinstein, J. L., Fleet, D. J. & Brubaker, M. A. cryoSPARC: algorithms for rapid unsupervised cryo-EM structure determination. *Nat. Methods* **14**, 290–296 (2017).

41. Bepler, T. *et al.* Positive-unlabeled convolutional neural networks for particle picking in cryo-electron micrographs. *Nat. Methods* **16**, 1153–1160 (2019).

42. Jumper, J. *et al.* Highly accurate protein structure prediction with AlphaFold. *Nature* **596**, 583–589 (2021).

43. Pettersen, E. F. *et al.* UCSF ChimeraX: Structure visualization for researchers, educators, and developers. *Protein Sci. Publ. Protein Soc.* **30**, 70–82 (2021).

44. Emsley, P. & Cowtan, K. Coot: model-building tools for molecular graphics. *Acta Crystallogr. D Biol. Crystallogr.* **60**, 2126–2132 (2004).

45. Lugmayr, W. *et al.* StarMap: a user-friendly workflow for Rosetta-driven molecular structure refinement. *Nat. Protoc.* **18**, 239–264 (2023).

46. Liebschner, D. *et al.* Macromolecular structure determination using X-rays, neutrons and electrons: recent developments in Phenix. *Acta Crystallogr. Sect. Struct. Biol.* **75**, 861–877 (2019).

47. The PyMOL Molecular Graphics System, Version 2.5 Schrödinger, LLC. https://pymol.org/2/support.html?#citing.

48. Briones, R., Blau, C., Kutzner, C., de Groot, B. L. & Aponte-Santamaría, C. GROmaρs: A GROMACS-Based Toolset to Analyze Density Maps Derived from Molecular Dynamics Simulations. *Biophys. J.* **116**, 4–11 (2019).

49. Kirchweger, P. *et al.* Structural and functional characterization of SiiA, an auxiliary protein from the SPI4-encoded type 1 secretion system from Salmonella enterica. *Mol. Microbiol.* **112**, 1403–1422 (2019).

50. Batth, T. S. *et al.* Protein Aggregation Capture on Microparticles Enables Multipurpose Proteomics Sample Preparation*. *Mol. Cell. Proteomics* **18**, 1027–1035 (2019).

51. Cox, J. & Mann, M. MaxQuant enables high peptide identification rates, individualized p.p.b.-range mass accuracies and proteome-wide protein quantification. *Nat. Biotechnol.* **26**, 1367–1372 (2008).

52. The UniProt Consortium. UniProt: the Universal Protein Knowledgebase in 2023. *Nucleic Acids Res.* **51**, D523–D531 (2023).

53. Chi, H. *et al.* Comprehensive identification of peptides in tandem mass spectra using an efficient open search engine. *Nat. Biotechnol.* (2018) doi:10.1038/nbt.4236.

54. Röst, H. L. *et al.* OpenMS: a flexible open-source software platform for mass spectrometry data analysis. *Nat. Methods* **13**, 741–748 (2016).

55. Tyanova, S. *et al.* The Perseus computational platform for comprehensive analysis of (prote)omics data. *Nat. Methods* **13**, 731–740 (2016).

56. Schmidt, A. *et al.* The quantitative and condition-dependent Escherichia coli proteome. *Nat. Biotechnol.* **34**, 104–110 (2016).

57. Ducret, A., Quardokus, E. M. & Brun, Y. V. MicrobeJ, a tool for high throughput bacterial cell detection and quantitative analysis. *Nat. Microbiol.* **1**, 1–7 (2016).

58. Schindelin, J. *et al.* Fiji - an Open Source platform for biological image analysis. *Nat. Methods* **9**, 10.1038/nmeth.2019 (2012).

59. One-way ANOVA followed by Dunnett's multiple comparisons test was performed using GraphPad Prism version 9.0.0 for Mac OS X, GraphPad Software, Boston, Massachusetts USA, www.graphpad.com.

60. Haft, D. H. *et al.* RefSeq: an update on prokaryotic genome annotation and curation. *Nucleic Acids Res.* **46**, D851–D860 (2018).

61. Mirdita, M. *et al.* ColabFold: making protein folding accessible to all. *Nat. Methods* **19**, 679–682 (2022).

62. Evans, R. *et al.* Protein complex prediction with AlphaFold-Multimer. 2021.10.04.463034 Preprint at https://doi.org/10.1101/2021.10.04.463034 (2022).

1167   63. Edgar, R. C. Muscle5: High-accuracy alignment ensembles enable unbiased assessments of
1168   sequence homology and phylogeny. *Nat. Commun.* **13**, 6968 (2022).

1169   64. Adobe Illustrator. *PCMag UK* https://uk.pcmag.com/illustration/9711/adobe-illustrator (2021).

1170   65. Pravda, L. *et al.* MOLEonline: a web-based tool for analyzing channels, tunnels and pores
1171   (2018 update). *Nucleic Acids Res.* **46**, W368–W373 (2018).

1172   66. Jurrus, E. *et al.* Improvements to the APBS biomolecular solvation software suite. *Protein Sci.*
1173   *Publ. Protein Soc.* **27**, 112–128 (2018).

1174   67. Perez-Riverol, Y. *et al.* The PRIDE database resources in 2022: a hub for mass spectrometry-
1175   based proteomics evidences. *Nucleic Acids Res.* **50**, D543–D552 (2022).

1176   68. Matias, V. R. F., Al-Amoudi, A., Dubochet, J. & Beveridge, T. J. Cryo-Transmission Electron
1177   Microscopy of Frozen-Hydrated Sections of Escherichia coli and Pseudomonas aeruginosa. *J.*
1178   *Bacteriol.* **185**, 6112–6118 (2003).

1179

Data and Code Availability

Atomic coordinates for ZorAB WT, ZorA$^{E86A/E89A}$ZorB, ZorA$^{\Delta359-592}$ZorB and ZorA$^{\Delta435-729}$ZorB were deposited in the Protein Data Bank (PDB) under accession codes 8QYD, 8QYH, 8QYK, 8QYY, respectively. The corresponding electrostatic potential maps were deposited in the Electron Microscopy Data Bank (EMDB) under accession codes EMD-18751, EMD-18754, EMD-18756, EMD-18766, respectively. The local refinement map of ZorB PGBD in ZorAB WT were deposited in the EMDB under accession codes EMD-18752. Atomic coordinates for ZorC were deposited in the PDB under accession codes PDB: 8R68. The corresponding electrostatic potential maps was deposited in the EMDB under accession codes EMDB: EMD-18848. Atomic coordinates for ZorD apo form and its complex with ATP-γ-S were deposited in the PDB under accession codes PDB: 8QY7 and 8QYC, respectively. The corresponding electrostatic potential maps were deposited in the EMDB under accession codes EMD-18747 and EMD-18750. The mass spectrometry proteomics data have been deposited to the ProteomeXchange Consortium via the PRIDE[67] partner repository with the dataset identifier PXD047450. Username: reviewer_pxd047450@ebi.ac.uk. Password: D7vNT520

Acknowledgements

1221 **Author contribution**

1222

1223 N.M.I.T. and H.H. conceived the project. H.H., A.R-E., and N.R. and F.J.O.M. did molecular
1224 biology and mutagenesis. H.H. expressed, purified, optimized, prepared cryo-EM grids, collected
1225 cryo-EM data, and determined all the structures presented in this study. S.A.J. and T.C.D.H.
1226 performed phage infectivity, adsorption, and phage burst assays. S.A.J. performed cell survival,
1227 conjugation, and transformation assays. L. J. P. performed bioinformatic analyses. P.F.P. carried
1228 out and analyzed TIRF experiments and together with M. E. interpreted the localization studies.
1229 F.J.O.M. and N.R. assisted with protein purification. F.J.O.M., N.R., and H.H. optimized the
1230 nuclease and EMSA experiments. A.R-E. and V K.D.S. purified phage genomes. Y.W. and Y.Y.
1231 helped with ZorA tail structure modeling. H. H. prepared samples for mass spectrometry. I. A. H.
1232 and M. L. N. performed mass spectrometry and analyzed the data. H.H. prepared figures and wrote
1233 the first draft of the manuscript together with N.M.I.T. and S.A.J. with input from all the authors.
1234 This draft was then edited by M.E., P.F.P. and R.B., and all the other authors. All authors
1235 contributed to the revision of the manuscript.
1236

1237 **Competing Interests**

1238

1239 The authors declare no competing interests.

1240

1241

Figure Legends:

Figure 1. Zorya has broad activity against phages via a direct immunity mechanism.

a, Zorya phylogenetic tree. As ZorA and ZorB are present in all Zorya types, the tree was generated using concatenated ZorA+B sequences. The outer ring represents the Zorya types I, II or III, and the inner ring represents the taxonomy of bacteria. The taxonomic rank being highlighted is at the phylum level. On the right, the gene organization of the three Zorya types is shown. **b**, *Ec*ZorI defense against diverse *E. coli* phages, determined using efficiency of plaquing (EOP) assays. AAI: Average amino acid identity. **c**, Adsorption of phage Bas24 to *E. coli* cells possessing or lacking *Ec*ZorI. **d**, One-step phage growth curve for phage Bas24 infecting *E.coli*, with or without *Ec*ZorI, normalized to the plaque forming units (PFU) per mL at the initial timepoint. **e**, Infection time courses for liquid cultures of *E. coli*, with and without *Ec*ZorI, infected at different multiplicities of infection (MOI) of phage Bas24. **f**, Phage titers at the end timepoint for each sample from the infection time courses (e), measured as EOP on indicator lawns of *E. coli* either without (control) or with *Ec*ZorI. The limit of detection (LOD) is shown with dotted lines. **g**, Survival of *E. coli* cells, lacking or possessing *Ec*ZorI, infected at an MOI of 5 with Bas24. In panels **b-d**, data represent the mean of at least three replicates and error bars (**c,d**) or shaded regions (**e**) represent the standard error of the mean (SEM).

Figure 2. Cryo-EM of *Ec*ZorAB and its architecture.

a, Schematic representation of *Ec*ZorA and *Ec*ZorB. **b,** Negative staining image of purified *Ec*ZorAB particles. **c**, Representatives of high-resolution 2-dimensional classes of *Ec*ZorAB particles from cryo-EM. Domain architectures of the E*c*ZorAB complex are depicted. **d**, Cryo-EM map of *Ec*ZorAB. Five ZorA subunits (purple, salmon, light green, tan, and coral) surround two ZorB subunits (white and dark gray) viewed from the plane of the membrane. Membrane-bound lipids are shown in yellow. The detergent micelle is shown as a translucent surface representation in cyan. Dashed lines depict inner membrane boundaries. **e**, Cross-section view of the EM density map. **f**, Ribbon model representation of *Ec*ZorAB. **g**, Structure of a single ZorA subunit. **h-i**, Cross-section view of the Cryo-EM map of *Ec*ZorAB TMD (**h**) and tail (**i**) from the periplasmic side. **j-k**, Cross-section view of the model of *Ec*ZorAB TMD (**j**) and tail (**k**) from the periplasmic side. **l**, Composite model of *Ec*ZorAB whole complex. the predicted portion of the ZorA tail is represented as surface. The radius of the ZorA tail is shown in **l**. PP, periplasm; IM, inner membrane; CP, cytoplasm; PGBD, peptidoglycan binding domain; TMD, transmembrane domain; MPCD, membrane-proximal cytoplasmic domain; TM, transmembrane; H, helix.

Figure 3. ZorAB is a PG-binding rotary motor.

a, *Ec*ZorAB viewed from the plane of the membrane, with ZorB shown as ribbons (black and white) and ZorA shown as a translucent surface representation. The distance between the inner membrane and PG layer in *E.coli* is approximately 90 Å[68]. The cysteines from the two disulfide bridges in the ZorB PGBD are indicated and shown as spheres. The aspartate residues D26 from

1282 both ZorB TM are indicated and shown. **b**, Top view of the ZorB PGBD. **c,** Close-up view of the
1283 interactions of ZorB with ZorA at the domain assembly interface in the periplasmic space. **d,** Cross
1284 section view of ZorAB TMD, showing the ZorB D26 and surrounding residues. **e**, Ca^{2+} binding
1285 site. EM densities are only overlapped on Ca^{2+} ion, and the two water molecules. **f**, Close-up view
1286 of the interactions of the ZorB N-terminus with ZorA tail **g**, Ion translocation pathway
1287 (semitransparent surface representation in light blue) in ZorAB. Residues along the ion permeation
1288 pathway and from the ion selectivity filter are shown. Each asterisk indicates residues or structural
1289 elements from neighboring ZorA subunit. **h**, The effects of ZorA and ZorB mutations on *Ec*ZorI-
1290 mediated anti-phage defense, as measured using EOP assays. Data represent the mean of at least
1291 3 replicates and are normalized to the control samples lacking *Ec*ZorI. For phage Bas58, the limit
1292 of detection (LOD; one plaque observed in the assay) is marked with a bashed line. In the absence
1293 of any observed plaques, the result was recorded as the LOD. ZorB$^{46-52>GGGSGGS}$ corresponds to
1294 the replacement of ZorB residues 46-52 with a GGGSGGS linker. Data for additional phages are
1295 provided in **Extended Data Fig. 6a.**

1296

1297 **Figure 4. Structural and functional characterization of ZorC and ZorD.**
1298 **a**, Ribbon model representation of ZorC. **b**, Details of the ZorC EH signature motif. **c**, The effects
1299 of ZorC mutations on *Ec*ZorI-mediated anti-phage defense, as measured using EOP assays. **d**, *In*
1300 *vitro* interaction of *Ec*ZorC with 200 nM dsDNA (52bp, 5' FAM-labeled scrambled DNA
1301 sequence), ZorC concentrations were from lane 2 to lane 8: 1600, 100, 200, 300, 500, 1000, and
1302 1600 nM, respectively. **e**, The effects of ZorC mutations on dsDNA binding activity, all reactions
1303 were made to a final concentration of 200 nM of dsDNA and 1000 nM of protein. Gels in **d** and **e**
1304 are representative of three independent assays. **f**, Ribbon model representation of *Ec*ZorD in
1305 complex with ATP-γ-S. *Ec*ZorD structure is shown in light purple with the bound ATP-γ-S shown
1306 in spheres. **g**, The ZorD ATP-γ-S binding site. The backbone of the DEAQ box motif (ZorD
1307 residues 730-733) is colored in magenta. Conserved negatively charged residues surrounding ZorD
1308 DEAQ box motif is shown. **h**, The effects of ZorD mutations on *Ec*ZorI-mediated anti-phage
1309 defense, as measured using EOP assays. ΔNTD represents ZorD$^{Δ1-502}$ and ΔCTD represents
1310 ZorD$^{Δ503-1080}$. **i**, ZorD$_{CTD}$ degrades linear plasmid DNA. **j-l**, ZorD$_{CTD}$ degrades phage genomic
1311 DNA (gDNA). For c and h, data represent the mean of at least 3 replicates and are normalized to
1312 the control samples lacking *Ec*ZorI. For phage Bas58, the limit of detection (LOD; one plaque
1313 observed in the assay) is marked with a bashed line. Data for additional phages are provided in
1314 **Extended Data Fig. 6a**. **6d**, **6e** and **i-l** are representative of at least 3 replicates.

1315

1316 **Figure 5. ZorAB recruits ZorC and ZorD during phage invasion.**
1317 **a**, **c**, **e,** Exemplary deconvolved TIRF microscopy pictures of ZorB C-terminal, ZorC N-terminal,
1318 and ZorD C-terminal fusions with mNeongreen either untreated or exposed to Bas24 at an MOI of
1319 5 for 30 min. **b, d, f,** Comparison of detected maxima of the ZorI proteins between untreated or
1320 exposed to Bas24 at an MOI of 5 for 30 min (n cells > 250). Means are derived from three
1321 independent biological replicates. Scale bar 2 μm. Statistics were calculated in Prism GraphPad 9

1322 by applying the in-built analyses of unpaired t-tests or one-way ANOVA[59]. P-value: NEJM (New
1323 England Journal of Medicine) style, 0.12 ns, 0.033(*), 0.002(**), <0.001(***).
1324
1325 **Figure 6. Proposed model of Zorya activation.**
1326 **a**, An inactive ZorAB complex embedded in the inner membrane. **b-c**, Inactive ZorAB complex
1327 detects a signal from phage infection that (**b**) depresses the cell wall or (**c**) induces inner membrane
1328 curvature. ZorB PGBDs binds and anchors to the cell wall. Ion translocation through activated
1329 ZorAB generates rotational torque, triggering ZorA and its long intracellular tail to rotate around
1330 ZorB. **d**, The signal from the ZorAB motor is transferred through the ZorA tail, which recruits
1331 and/or activates ZorC and ZorD. Activated ZorC/D binds phage DNA, restricting it to a zone close
1332 to the site of phage genome injection, where nuclease degradation of phage DNA prevents phage
1333 infection.
1334

Extended Data Legends:

Extended Data Figure 1. *E. coli* **Zorya type I protects against phage invasion but not bacterial conjugation or plasmid transformation.**
a, The impact of *Ec*ZorI on the uptake of plasmid DNA via conjugation from an *E. coli* donor strain, measured as the transconjugant frequency (number of transconjugants/total recipients). Four plasmids with different origins of replication (OriV) were tested (ColE1, RSF1010, pBBR1 and RK2), at the indicated donor to recipient cell ratios (D:R) for the matings. Data represent the mean of three replicates. **b**, The impact of *Ec*ZorI on the uptake of plasmid DNA via transformation. Chemically competent *E. coli* without (control; empty vector) or with *Ec*ZorI were transformed with plasmids possessing either ColE1 or pBBR1 origins of replication. Data represent the mean of three replicates, with each replicate being a different batch of competent cells. **c**, Infection time courses for liquid cultures of *E. coli*, with and without *Ec*ZorI, infected at different multiplicities of infection (MOI) of phage Bas02 and Bas08. **d**, Phage titers at the end timepoint for each sample from the infection time courses (**c**), measured as EOP on indicator lawns of *E. coli* either without (control) or with *Ec*ZorI. LOD: Limit of detection.

Extended Data Figure 2. Cryo-EM dataset processing results and resolution of *Ec*ZorAB.
a, A representative SDS gel of the purified *Ec*ZorAB complex. **b**, An EM image of the *Ec*ZorAB sample under the cryogenic conditions. **c**, Cryo-EM density map of *Ec*ZorAB colored by local resolution (in Å) estimated in cryoSPARC with gold standard (0.143) Fourier Shell Correlation (GSFSC) curves. **d**, Cryo-EM map of *Ec*ZorAB. **e-g**, Representative model segments of ZorA and non-residual molecules fitted into EM density, focusing on one of ZorA subunit's TM1, and lipids found in the TMD of ZorA. **h-i**, Strategy of the local refinement of the ZorB PGBDs with a soft mask. **j**, A representative of a model segment of the ZorB PGBDs fitted into EM density map, focusing on the PGBD dimerized interface. **k**, Volcano plot analysis, visualizing ratio and significance of change between all proteins quantified by mass spectrometry in *E. coli* total lysates either transformed with p*Ec*ZorI plasmids or not (**Extended Data Table 2**). Significance was tested via two-tailed two-sample Student's t-testing with permutation-based FDR control, ensuring a corrected p-value of < 0.01. n=4 technical replicates derived from n=3 culture replicates. **l**, Absolute copy-number analysis of Zorya proteins expressed in *E. coli*. Determined via comparison of molecular weight-adjusted label-free quantified protein abundance values from this study, to known copy-numbers reported by Schmidt et al.[56], and establishing a "proteomic ruler" for conversion of measured abundance values to approximate copy-numbers (**Extended Data Table 2**). n=4 technical replicates derived from n=3 culture replicates.

Extended Data Figure 3. *Ec*ZorA tail secondary structural prediction and a complete composite model of *Ec*ZorAB complex.
a, Amino acids and secondary structural predictions (Psipred) of the *Ec*ZorA. The peptides found by mass spectrometry that covered ZorA protein are indicated as green lines about the amino acids.

1375 **b,** Top hits from an HHpred sequence homology search of the ZorA tail are shown. **c**, A composite
1376 model of *Ec*ZorAB with the ZorA tail folding into a pentameric super coiled-coil, with the helical
1377 pitch of the tail α-helix shown. **d**, Hydrophobicity and polarity of the inner surface of the ZorA tai
1378 calculated by MOLE*online*.
1379
1380 **Extended Data Figure 4. *Ec*ZorAB is a peptidoglycan binding rotary motor.**
1381 **a**, Cartoon representation of the *Ec*ZorAB complex in an inactive state, with the ZorB dimerized
1382 interfaced highlighted. **b**, Topology diagrams of ZorB and isolated crystal structures of the
1383 flagellar stator unit MotB and PomB PGBDs, indicating a conserved folding architecture. **c-d**, The
1384 two disulfate bonds identified from ZorB PGBDs, with the EM map overlapped. **e**, Pull-down
1385 assay of the isolated *Ec*ZorAB complex with the purified peptidoglycan. **f**, Cartoon representation
1386 of the cryo-EM structure of the proton-driven flagellar stator unit MotAB from *Campylobacter*
1387 *jejuni* (*Cj*MotAB) in its inactive state, with the MotB plug motif highlighted. **g**, Cartoon
1388 representation of the cryo-EM structure of the sodium-driven flagellar stator unit PomAB from
1389 *Vibrio alginolyticus* (*Va*PomAB) in its inactive state. **h**, Cross-section view of the *Ec*ZorAB TMD,
1390 showing the surrounding residues of the two Asp26 from ZorB. **i**, Cross-section view of the
1391 *Cj*MotAB TMD, showing the surrounding residues of the two Asp22 from MotB. **j**, Cross-section
1392 view of *Va*PomAB TMD, showing the surrounding residues of the two Asp24 from PomB. The
1393 absence of the strictly conserved threonine residue on ZorA TM3 required for sodium ion binding,
1394 indicates that *Ec*ZorAB is a proton-driven stator unit. **m**, A representative of an SDS gel of the
1395 purified *Ec*ZorAB linker mutant complex (with ZorB residues 46-52 replaced by a GGGSGGS
1396 linker: *Ec*ZorAB linker mutant). **n**, An EM image of *Ec*ZorAB linker mutant sample under the
1397 cryogenic conditions. **o**, Representatives of the 2D classes of the *Ec*ZorAB linker mutant in
1398 comparison with that of the *Ec*ZorAB wild type, highlighting the flexibility of the ZorB PGBDs
1399 of the *Ec*ZorAB linker mutant. **p**, Low pass filter of the Cryo-EM density map of the *Ec*ZorAB
1400 linker mutant after nonuniform refinement. **q**, Transmembrane helix density of the *Ec*ZorAB linker
1401 mutant and that in the wild type *Ec*ZorAB.
1402
1403 **Extended Data Figure 5. Cryo-EM dataset processing and structures of the *Ec*ZorAB tail**
1404 **and Ca^{2+} binding site mutations.**
1405 **A**, Mutations of the ZorA tail truncations indicated in the composite model of *Ec*ZorAB complex.
1406 **B**, Interaction between the beginning of the ZorA tail and the β-hairpin motif. **C**, Extra density
1407 found inside the tail from cryo-EM map, which was modeled as palmitic acid, with the amino acids
1408 involved in the interactions indicated. **d**, Structural comparison of the ZorA wild type (cyan) and
1409 ZorA Ca^{2+} binding site mutation (ZorA$^{E86A/E89A}$, gray), the arrows highlight the changes from wild
1410 type to the mutant. **e**, Representative of the 2D classes of the *Ec*ZorAB ZorA tail complete deletion.
1411 **f**, Negative staining images of the *Ec*ZorAB wild type, ZorA tail middle deletion (ZorA$^{Δ359-592}$),
1412 ZorA tail tip deletion (ZorAΔ$^{435-729}$). **g**, The tail lengths of the *Ec*ZorAB wild type, ZorA tail
1413 middle deletion (ZorA$^{Δ359-592}$), ZorA tail tip deletion (ZorA$^{Δ359-592}$) as measured in (**f**). **h-j**, Cryo-

1414 EM maps and resolutions of ZorA mutants with gold standard (0.143) Fourier Shell Correlation
1415 (GSFSC) curves.
1416

1417 **Extended Data Figure 6. The effects of *Ec*Zorya mutations on *Ec*ZorI-mediated anti-phage**
1418 **defense and long ZorA tails are conserved amongst Zorya system types in diverse species.**
1419 **a**, The effects of ZorA, ZorB, ZorC and ZorD mutations on *Ec*ZorI-mediated anti-phage defense,
1420 as measured using EOP assays with phages Bas02, Bas19 and Bas25. Data represent the mean of
1421 at least 3 replicates and are normalized to the control samples lacking *Ec*ZorI. **b**, The ZorA tail
1422 lengths found in different Zorya system types. Motor and tail lengths were determined by
1423 inspecting the predicted structures of several representative ZorA sequences, then inferring these
1424 lengths for the rest of the ZorA sequences through sequence alignment (methods). The reduce
1425 sequencing bias, unique Zorya systems encoded in RefSeq (v209) bacteria and archaea genomes
1426 were selected based on their distinct genomic context (methods).
1427

1428 **Extended Data Figure 7. Cryo-EM dataset processing results and functional investigation of**
1429 ***Ec*ZorC.**
1430 **a**, Representative of the SDS gel of the purified ZorC wild type, ZorC^{E400A}, ZorC^{H443A}, ZorC$^{\Delta CTD}$
1431 (deletion residues 487-560). **b**, Representatives of the 2D classes of the *Ec*ZorC. **c**, Unsharpened
1432 Cryo-EM map of *Ec*ZorC with gold standard (0.143) Fourier Shell Correlation (GSFSC) curves
1433 shown below. **d**, Local refinement of the *Ec*ZorC core domain with a soft mask, with the local
1434 resolution (in Å) estimated in cryoSPARC. **e**, Representative of a model and segments of the ZorC
1435 fitted into EM density map. **f**, Final model of *Ec*ZorC built from cryo-EM map. **g**, AlphaFold2-
1436 predicted ZorC model. **h**, Electrostatic distribution of *Ec*ZorC calculated from AlphaFold2-
1437 predicted model.
1438

1439 **Extended Data Figure 8. Cryo-EM dataset processing results and resolutions of *Ec*ZorD and**
1440 ***Ec*ZorD in complex with ATP-γ-S.**
1441 **a**, Representative of the SDS gel of the purified ZorD wild type, ZorD$_{CTD}$ (residues 503-1080),
1442 ZorD$_{NTD}$ (residues 1-502), ZorD$_{CTD}$$^{D730A/E731A}$ and ZorD$_{CTD}$^{E651A}. Gel is representative of at least
1443 3 replicates. **b**, Unsharpened cryo-EM map of the *Ec*ZorD apo from with gold standard (0.143)
1444 Fourier Shell Correlation (GSFSC) curves shown below. **c**, Local refinement of the *Ec*ZorD apo
1445 form with a soft mask. **d**, Cryo-EM map of *Ec*ZorD in complex with ATP-γ-S. **e**, Structural model
1446 of the *Ec*ZorD in complex with ATP-γ-S. **f**, Structural comparison of the *Ec*ZorD apo from (gray)
1447 and *Ec*ZorD in complex with ATP-γ-S (light purple); the arrows highlight the changes from apo
1448 form to the ligand-bound form. **g**, Zoomed-in view of the ATP-γ-S binding site, with the cryo-EM
1449 map overlaid on the ATP-γ-S.
1450

1451 **Extended Data Figure 9. Complementation experiment between *E. coli* and *P. aeruginosa***
1452 **ZoryaI.**

a, Schematic representation of *Ec*ZorI, *Pa*ZorI and the constructs for *Pa*ZorCD or *Pa*ZorD complementation of *Ec*ZorI gene deletions. **b**, Anti-phage defense provided by the constructs in (**a**), as measured using EOP assays for phages Bas49, Bas52 and Bas57. Data represent the mean of at least 3 replicates and are normalized to the control samples lacking Zorya.

Extended Data Figure 10. ZorD recruitment during phage invasion at increasing MOIs and mNeongreen localization upon phage exposure.

a, The effects of the mNeongreen (mNG) fusions to *Ec*ZorI components on anti-phage defense, as measured using EOP assays for phages Bas02, Bas08, Bas19, Bas24, Bas25 and Bas58. Data represent the mean of at least 3 replicates and are normalized to the control samples lacking *Ec*ZorI. The boxed constructs (ZorB C-terminal mNG fusion: ZorB-mNG; ZorC N-terminal mNG fusion: mNG-ZorB; ZorD C-terminal mNG fusion: ZorD-mNG) were used for subsequent microscopy experiments. **b**, Exemplary denoised TIRF and brightfield microscopy pictures of mNeongreen expression driven by the *Ec*ZorI native promoter (p-mNG) either untreated, exposed to T4 or Bas24 at an MOI of 5 for 30 min. Scale bar 2 μm. **c**, **e**, Exemplary denoised TIRF microscopy pictures of ZorD-mNG either untreated or exposed to increasing Bas24 or T4 MOIs of 1, 5, or 50 for 30 min. **d**, **f**, Statistical comparison of ZorD-mNG maxima between untreated and conditions stated in **c**, **e**. Means derive from at least three independent biological replicates. Scale bar 2 μm. Our data in **e** and **f** showed phage T4 infection did not result in a dose-dependent ZorD-mNG response.

Extended Data Figure 11. Structural prediction of the representative ZorAB complexes form different Zorya system types. a, The predicted dimerized ZorB PGBDs. **b**, The predicted ZorAB transmembrane motor complex. One ZorA subunit is highlighted.

Extended Data Fig. 12. Proposed ZorA tail untwisting and phage DNA 'reeling in' mechanism in the activated Zorya defense system.

a, An inactive ZorAB embedded in the inner membrane. **b,** Phage invasion triggers ZorAB activation. The rotation of ZorA and its long intracellular tail around ZorB causes untwisting of the ZorA tail, which would recruit ZorC and ZorD**. c,** Reeling in of phage DNA around the long ZorA tail in the activated Zorya defense system. Legend Discussion: The 'reeling in' mechanism would greatly enhance phage genome localization and sequester it from interactions required for host infection. A typical double-stranded DNA phage genome is 10s of μm long, and would form a random coil with a radius of gyration similar to the size of the entire cell in the absence of constraints – thus negating any advantage of a localized nuclease defense response at the site of entry. Binding to multiple Zor complexes, perhaps via ZorC and/or D might contribute to localizing phage DNA to the entry site. Unless and until tail rotation is resisted, an almost inevitable consequence of tail rotation combined with DNA binding is that the DNA will wind around the tail like wire on a reel. If 'reeling in' of the phage DNA were an essential feature of the Zorya defense mechanism, this would explain the need for both rotation and a long ZorA tail. The

1493   length of the ZorA tail is very similar to that of a typical phage capsid into which an entire phage
1494   genome can (only just) be tightly packed, indicating that a single Zor complex may be sufficient
1495   to capture an entire genome. Rough calculations indicate that 100s of turns would be required to
1496   wind a 60 kb Bas24 genome onto a 70 nm tail, allowing the rotary ZorAB motor cumulatively to
1497   supply the necessary energy to wind and compact the phage DNA. Reeling would also tighten any
1498   loops that might form between DNA sites bound to different ZorA tails, removing any freedom
1499   for further ZorA rotation - as required by the model of activation via untwisting of the ZorA tail.

1500

1501 **Extended Data Tables**

1502

1503 **Extended Data Table 1**. **Cryo-EM data collection, refinement and validation statistics.**

1504

1505 **Extended Data Table 2. Mass Spectrometry analysis of the *E.coli* lysates with or without**
1506 **expression of the Zorya proteins.**

1507

1508 **Extended Data Videos**

1509

1510 **Extended Data Video 1 and Video 2.**

1511 **Exemplary deconvolved TIRF microscopy videos (1800 ms) of ZorB C-terminal fusion with**
1512 **mNeongreen.**

1513   *E. coli* expressing Zorya untreated with phage (**Video 1**) or exposed to Bas24 (**Video 2**) at an MOI
1514   of 5 for 30 min. The ZorAB complexes were predominantly membrane-localized and exhibited
1515   low diffusibility, irrespective of the absence or presence of phage (**Video 1**). Upon phage infection,
1516   the number of ZorAB foci increased (**Video 2**). Scale bar 2 μm.

1517

1518 **Extended Data Video 3 and Video 4.**

1519 **Exemplary deconvolved TIRF microscopy videos (1800 ms) of ZorD C-terminal fusion with**
1520 **mNeongreen**

1521   *E. coli* expressing Zorya untreated with phage (**Video 3**) or exposed to Bas24 (**Video 4**) at an MOI
1522   of 5 for 30 min. ZorD freely diffused in the cytoplasm in the absence of phage (**Video 3**). Upon
1523   phage infection, the number of ZorD foci increased and became static (**Video 4**). Scale bar 2 μm.

1524